Introduction to Nb-Based SQUID Sensors

Dietmar Drung

Physikalisch-Technische Bundesanstalt (PTB)
Abbestraße 2-12, 10587 Berlin, Germany

dietmar.drung@ptb.de

Abstract - **The superconducting quantum interference device (SQUID) is a highly sensitive detector for magnetic flux or any quantity that can be efficiently converted into flux. Comprehensive overviews of the fundamentals, technology and applications of SQUIDs and SQUID systems are found in the literature (for example [1-6]). In this paper, a short introduction into the basic function of a SQUID, its operation, and its design for magnetic field and current sensing is given. An extended version of this paper will appear in the forthcoming book "Josephson Junctions: History, Devices, and Applications" edited by E. L. Wolf, G. B. Arnold, M. A. Gurvitch, and J. F. Zasadzinski (Pan Stanford Publishing). Due to the focus of this book on Nb-based devices, the large field of devices with high critical temperature (high-T_c SQUIDs) will not be considered here.**

I. SQUID FUNDAMENTALS

A SQUID basically consists of a superconducting loop interrupted by one or more Josephson junctions. Depending on the number of junctions, it is named rf SQUID (one junction) or dc SQUID (two junctions), respectively. This classification results from the basic mode of operation: the rf SQUID is driven by a high-frequency signal (tens or hundreds of megahertz typically) applied to a tank circuit magnetically coupled to the SQUID, whereas the dc SQUID is biased with a direct current. The dc SQUID was discovered by Jaklevic *et al.* [7], only a few years after Josephson's predictions of superconducting tunneling. The rf SQUID was introduced shortly afterwards [8]. In those days, it was extremely difficult to fabricate reliable Josephson junctions with thin-film techniques. As a result, early SQUIDs were equipped with "point contacts" consisting of a Nb screw pressed against a Nb body, thereby forming an adjustable Josephson junction.

It is obviously much more demanding to obtain two point contacts with similar parameters than to adjust only one. Therefore, although the dc SQUID generally allows a lower overall noise, the rf SQUID became the standard device in the following years. The situation changed after reliable thin-film processes were developed in the 1970s and 1980s, and the dc SQUID began to replace the rf SQUID. Nowadays, the dc SQUID is dominant in the field of Nb-based sensors, and the rf SQUID is practically obsolete. Therefore, this chapter deals with the

dc SQUID only; the rf SQUID is extensively discussed in literature (see for example [4]).

A.   Basic SQUID Function

The dc SQUID is based on two effects: flux quantization and superconducting tunneling. Its function is schematically illustrated in Fig. 1. The most simple circuit is assumed: a superconducting loop interrupted by two Josephson junctions. The junctions have parallel-connected resistors R to eliminate hysteresis in their current-voltage characteristics [9,10]. We first consider the case in Fig. 1(a) where a quasi-static current I is passed through the SQUID but no magnetic field is applied. Due to symmetry, the current splits into two equal halves $I/2$ that flow through the two Josephson junctions. The corresponding current-voltage characteristic is shown in Fig. 1(c). Neglecting noise rounding, the total critical current of the SQUID $2I_c$ is the sum of the two junction critical currents I_c.
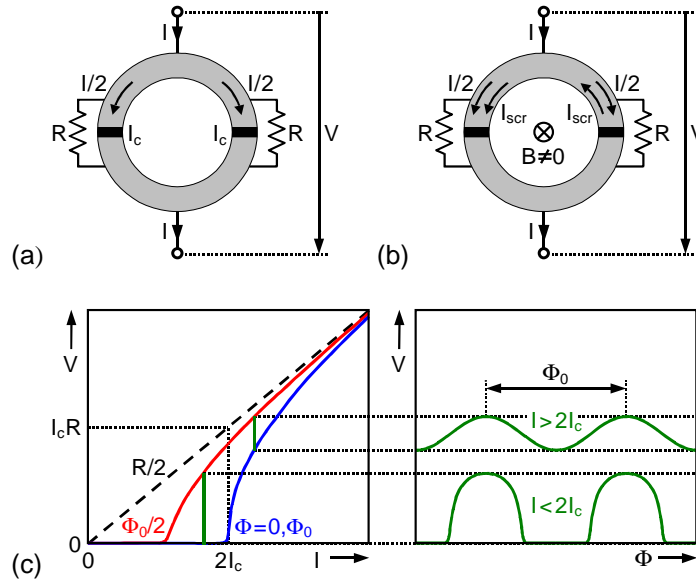
Fig. 1. Basic SQUID circuit with (a) zero and (b) nonzero applied magnetic flux density B. The resulting voltage-current and voltage-flux characteristics are schematically shown in (c). The dashed line shows the resistance that would be obtained without tunneling. To remove hysteresis in their characteristics, the two Josephson junctions (black regions incorporated into the superconducting loop) are shunted by resistors R connected in parallel.

If a magnetic field is applied perpendicular to the SQUID loop, the resulting flux in the loop $\Phi = BA$ (assuming that the flux density B is constant over the area A of the loop) will cause a screening current I_{scr} to circulate. As we will see later, the Josephson junctions are commonly made as small as possible, so that the effect of the applied field on the junction critical currents can be neglected. For the example in Fig. 1(b), the screening current is added to $I/2$ in the left junction, but subtracted from $I/2$ in the right one. Therefore, the critical current of the left junction is already reached at $I/2 < I_c$ and hence the critical current of the SQUID is reduced with applied flux. If the magnetic flux caused by the screening current exceeds $\pm\Phi_0/2$, the flux state of the SQUID changes by one flux quantum $\Phi_0 \approx 2.068 \times 10^{-15}$ Vs and the screening current changes its direction because this is energetically more favorable than a further increase in the screening current. This way, the total flux in the loop is always kept equal to an integer number of flux quanta (flux quantization) and the

critical current of the SQUID changes periodically with the applied flux.

As illustrated in Fig. 1(c), the flux dependence of the critical current leads to a periodic voltage-flux characteristic if the SQUID is biased at constant current I. The period is exactly equal to one flux quantum Φ_0. For $I \leq 2I_c$, the zero-voltage state is included in the voltage-flux characteristic, whereas for $I > 2I_c$ the SQUID is always in the voltage state with a finite dc voltage across the device. Note that in the voltage state, due to the ac Josephson effect, a high-frequency ac voltage is always superimposed with a fundamental of 483.6 MHz per microvolt of dc voltage. In Fig. 1 it was assumed that this ac Josephson voltage is outside the measurement bandwidth and filtered out by the measurement setup (which is always the case in practice). Finally, in the above discussion we have neglected thermal noise. In practice, the characteristics in Fig. 1 are rounded near zero voltage due to thermal noise.

The SQUID function is determined by four basic quantities: the inductance of the SQUID loop L, the junction critical current I_c, the shunt resistance per junction R, and the parasitic junction capacitance C. The tunnel junctions may be intrinsically shunted or equipped with parallel-connected resistors. Strictly speaking, in the latter case the quasiparticle tunneling would slightly contribute to the effective shunt resistance R; however, this effect is commonly negligible. The specific junction capacitance is relatively high because of the plate-capacitor-like structure with the very thin (a few nanometers typically) tunnel barrier between the electrodes. For window-type junctions, C includes the effect of the overlap area around the tunnel barrier. For cross-type junctions, the overlap contribution is practically eliminated [11]. Extremely small junctions are used in nanometer-sized SQUIDs, the so-called nanoSQUIDs [12]. Here, the parasitic capacitance from the vicinity of the junctions can dominate the total capacitance.
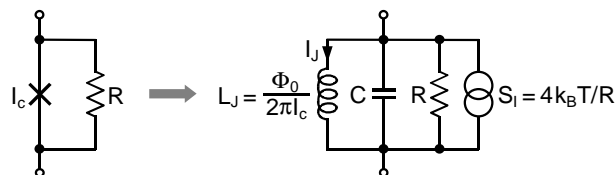
Fig. 2. Simplified equivalent circuit of a resistively-shunted junction with small Josephson tunnel current $I_J \ll I_c$. The effect of superconducting tunneling was approximated by an inductance $L_J = \Phi_0/(2\pi I_c)$.

The SQUID is a strongly nonlinear device. Analytical solutions for the corresponding mathematical equations are available in a few special cases only, but unfortunately for parameters less suitable for practical devices. Intensive computer simulations were performed beginning in the mid 1970s to understand the device and to find design rules for optimum SQUID function [1,13-16]. These simulations yielded conditions for the three major SQUID parameters that will be discussed and made plausible here on the basis of the simplified junction circuit depicted in Fig. 2. For small supercurrents $I_J \ll I_c$ through the tunnel junction, the sine function in the dc Josephson effect can be approximated by the linear term of its Taylor series. As a result, in this case the effect of superconducting tunneling can be taken into account by an equivalent inductance $L_J = \Phi_0/(2\pi I_c)$. For larger tunnel currents I_J approaching $\pm I_c$, the higher-order terms in the sinusoidal current-phase relation become dominant. Therefore, the effective inductance increases nonlinearly with I_J, becomes infinite at $I_J = \pm I_c$ and even negative if I_J exceeds $\pm I_c$. This clearly shows that the device dynamics are

very complicated. However, the simplified circuit in Fig. 2 is helpful for understanding some basic relationships.

Thermal noise in the shunt resistance can be taken into account by a current source in parallel to the junction having a power spectral density $S_I = 4k_B T/R$, where $k_B \approx 1.38 \times 10^{-23}$ J/K is the Boltzmann constant and T is the absolute temperature. Integrating over frequency, the total rms noise current flowing through L_J is found to be $I_{J,rms} = (k_B T/L_J)^{1/2}$. Obviously, to avoid thermal noise "wiping out" the superconducting tunnel effect, it is required that $I_{J,rms} \ll I_c$. Thus we obtain a condition for the noise parameter

$$\Gamma = (I_{J,rms}/I_c)^2 = 2\pi k_B T/(\Phi_0 I_c) \ll 1 \quad . \tag{1}$$

The parameter Γ describes the rounding of the junction characteristics due to thermal noise and is a measure for the apparent reduction of the critical current in the presence of thermal noise [17]. For a typical critical current $I_c = 10$ μA, one obtains $L_J = 33$ pH and an rms noise current $I_{J,rms} = 1.33$ μA at liquid helium temperature ($T = 4.2$ K), resulting in $\Gamma \approx 0.018$. Eq. (1) is fulfilled at 4.2 K for critical currents above about 1 μA.

Due to the parasitic capacitance C, the Josephson junction forms a parallel resonant circuit. For the simplified circuit in Fig. 2 we find a quality factor $Q_J = R(C/L_J)^{1/2}$. Generally, it is advisable to keep the quality factor of resonant circuits in nonlinear systems below about unity to minimize excess noise from down-mixing effects. In the case of a Josephson junction, hysteresis occurs in the current-voltage characteristic for Q_J above about unity (without noise the hysteresis limit is $Q_J \approx 0.84$ [1]). Q_J can be set for given I_c and C by selecting R appropriately. However, R should not be chosen too low because this would result in a small peak-peak output voltage V_{pp} of the SQUID (typically $V_{pp} \approx 0.4\,I_c R$). Therefore, in practice a good compromise is

$$\beta_C = Q_J^2 = 2\pi I_c R^2 C/\Phi_0 \approx 1 \quad . \tag{2}$$

At 4.2 K and relatively low critical currents $I_c \approx 3.5$ μA (corresponding to $\Gamma \approx 0.05$) minimum SQUID noise is obtained for β_C between 1 and 2 [1]. In contrast, for very low $\Gamma < 0.01$ typically obtained at millikelvin temperatures, it is advisable to keep $\beta_C < 0.5$ to improve damping. This is particularly important if the effective junction capacitance is higher than expected due to parasitic capacitance in the SQUID layout [16]. Although a slight hysteresis in the SQUID characteristics might not be visible due to thermal noise, it can degrade the noise performance substantially at low values of Γ.

As discussed above, the flux-dependence of the critical current of the SQUID results from the screening current I_{scr} interacting with the Josephson junctions. Obviously, I_{scr} decreases with increasing SQUID inductance L. Thus, the modulation depth of the critical current and the resulting output voltage modulation ΔV are maximized for small SQUID inductance $L \ll L_J$. In the limit $L/L_J \to 0$, the critical current of the SQUID as a function of applied flux becomes $2I_c|\cos(\pi\Phi/\Phi_0)|$, i.e., it is completely suppressed at $\Phi = (n+\frac{1}{2})\Phi_0$ (n is an integer). However, simulations show that for too low L/L_J the SQUID noise increases, leading to the design rule [13]

$$\beta_L = L/(\pi L_J) = 2LI_c/\Phi_0 \approx 1 \quad . \tag{3}$$

Combining Eq. (3) with Eq. (1), one obtains a practical limit for the SQUID inductance $L_{max} \approx$

1 nH at 4.2 K.

The design rules Eqs. (2) and (3) are helpful guides in practice. One first selects the SQUID inductance according to the intended application (typically $L \approx 100$ pH) and assumes the smallest junction size to minimize capacitance (typically $C \approx 0.4$ pF). Next, Eq. (3) is used to determine I_c from the given L. With the help of Eq. (2) one obtains the required R and the resulting number of squares in the shunt resistor layout for the nominal sheet resistance of the shunt material (for example 4 Ω per square for 70 nm thick AuPd). The final optimization is preferably done during routine fabrication by fine-tuning the critical current density of the Josephson junctions and the film thickness of the shunt resistors.

B.   SQUID Noise

Achieving a low noise level is the most important issue in the field of SQUID sensors. As discussed above, the period in the voltage-flux characteristic is exactly equal to the flux quantum Φ_0. Therefore, the flux sensitivity of the SQUID is automatically "calibrated" and the measured output noise can easily be converted into $\Phi_0/\sqrt{\text{Hz}}$. However, in most cases the signal applied to the SQUID is not magnetic flux directly, but rather magnetic field or current, the latter being passed through a coil inductively coupled to the SQUID loop. In any case, it is necessary to specify the noise figure of the sensor in units of the quantity to be measured, for example the flux density in the pick-up coil B or the input current I_i. The corresponding power spectral densities are related to the flux noise density S_Φ by

$$S_B = S_\Phi/A_{\text{eff}}^2 \quad \text{or} \quad S_I = S_\Phi/M_i^2 \quad . \tag{4}$$

Here, A_{eff} is the effective field-sensitive area of the SQUID magnetometer; often, the inverse of A_{eff} in units of T/Φ_0 is referred to as field sensitivity. In the case of current sensing applications, M_i is the mutual inductance between the input coil and the SQUID loop.

The flux noise in the SQUID is caused by thermal noise in the shunt resistors, that is accounted for in Fig. 2 by the current source $S_I = 4k_B T/R$. As a result, the dc voltage V across the SQUID shows fluctuations V_N that are interpreted as fluctuations in flux $\Phi_N = V_N/V_\Phi$ ($V_\Phi = \partial V/\partial \Phi$ is the transfer coefficient at the chosen working point in the voltage-flux characteristic). It is important to note that the flux noise $\sqrt{S_\Phi}$ is a superposition of a "true" flux noise component (i.e., fluctuations in the screening current $I_{N,\text{scr}}$) and a voltage noise component that represents "apparent" flux noise only. When operating the SQUID as a high-frequency amplifier by coupling an input coil inductively to the SQUID loop, the noise in the screening current induces a noise voltage in the input coil [18,19]. This causes backaction of the SQUID on the signal source, makes the noise analysis more complicated, and can degrade the signal-to-noise ratio. Fortunately, in most SQUID applications this effect is small or even completely negligible, so that it is commonly sufficient to know the total flux noise density S_Φ only.

A useful figure of merit for characterizing SQUIDs is the noise energy per bandwidth ε referred to the SQUID inductance L. To derive it, we substitute the fluctuations in flux Φ_N by equivalent current fluctuations $I_N = \Phi_N/L$ and calculate the noise energy $LI_N^2/2 = \Phi_N^2/2L$. We then replace Φ_N^2 by the spectral density S_Φ and obtain the noise energy per bandwidth $\varepsilon = S_\Phi/2L$ that is often quoted in units of Planck's constant $h \approx 6.63\times10^{-34}$ J/Hz. For the near-optimum case $\beta_L \approx 1$ and $\beta_C \approx 1$ numerical simulations [13,14] yield the white noise level

$$\varepsilon_w \approx 9 k_B TL/R \quad \text{or} \quad \varepsilon_w \approx 16 k_B T (\text{LC})^{1/2} \quad . \tag{5}$$

Due to the strongly nonlinear SQUID characteristics and the "inherent local oscillator" (the Josephson ac voltage at typically 5 GHz with a rich spectrum of harmonics), thermal noise in the shunt resistors is mixed down from the microwave regime into the signal frequency range. A small-signal analysis without nonlinear effects yields $\varepsilon_w \approx 2 \, k_B TL/R$ [20], i.e., more than three-fourths of the noise energy in Eq. (5) are caused by down-mixing. Eq. (5) was obtained for a "bare" SQUID without including parasitic capacitance in the SQUID layout, for example due to a multiturn input coil coupled to the SQUID or the transmission line connecting the SQUID with the bonding pads. If parasitic high-Q resonant circuits in the SQUID design are driven by thermal noise, excess noise from down-mixing can become a severe problem and Eq. (5) can substantially underestimate the noise energy. Fortunately, in practice this excess noise can be strongly reduced by proper resonance damping, although the final noise energy will be always higher than without parasitic capacitance due to thermal noise in the damping resistors.

The general design rule for minimum noise energy is that parasitic capacitance should be kept as small as possible [16] and that, if parasitic resonant circuits cannot be avoided, appropriate damping by extra resistors or resistor-capacitor series shunts should be implemented [21-23]. This is particularly important when operating a SQUID at millikelvin temperatures because of the reduced noise level. At higher temperatures, hysteresis effects caused by parasitic capacitance are "wiped out" to a certain extend by thermal noise, which can somewhat relax the issue of resonance damping.

The white noise energy ε_w has a minimum when β_C is varied via the shunt resistance R for fixed SQUID inductance L and junction capacitance C. Below the optimum value of R, the noise energy degrades due to the increased thermal current noise $4k_B T/R$, while above optimum the down-mixing noise rises due to insufficient damping. The second expression in Eq. (5) shows a practical limit if L and C are fixed by SQUID layout and fabrication process. It assumes that R is optimally selected, typically near $\beta_C \approx 1$. The first expression in Eq. (5) can be used if R and L are given. It implies that the β_L is optimally chosen via the critical current I_c and that the junctions are sufficiently well damped. It is also applicable for strongly overdamped junctions with $\beta_C \ll 1$.

The white noise of well-designed Nb-based SQUIDs is typically in fair agreement with theory. Fig. 3 shows an example of a SQUID with strongly overdamped Josephson junctions ($\beta_C \approx 0.2$ and $\beta_L \approx 0.5$). The measured white noise energy of 28 h at 4.2 K is a factor of 1.75 above the value of 16 h calculated with Eq. (5) for $L = 110$ pH and $R = 5.4$ Ω, corresponding to a deviation of 32% in rms flux noise $\sqrt{S_\Phi}$. Cooling the SQUID to 310 mK improves the white noise energy by a factor of 12 to 2.3 h. Note that for operation at very low temperatures, the noise temperature of the shunt resistors (and correspondingly the SQUID noise) saturates at typically 300 mK due to self-heating (hot-electron effect [25]). Large cooling fins attached to the resistors improve the situation, but it is commonly difficult to reduce the effective resistor noise temperature below about 100 mK.

As observed in virtually all electronic devices (semiconducting as well as superconducting), also the SQUID noise rises at low frequencies. This additional low-frequency noise is called flicker noise or 1/f noise, the latter name resulting from the typical scaling of the power spectral density $S_\Phi \propto 1/f$. In contrast to the white noise, the low-frequency noise is less well understood and can generally not be predicted from the SQUID design. There are noise contributions from low-frequency critical current fluctuations that can

be suppressed by special modulation schemes involving bias reversal (for a review see chapter 4 in [4]). Fortunately, in contrast to high-T_c junctions, modern Nb-AlOx-Nb trilayer-based junctions show very small levels of critical current fluctuations and bias reversal schemes are commonly not required. This simplifies the readout electronics, which is helpful in particular for multichannel systems. However, there is another low-frequency noise component which reveals as a "true" flux noise and cannot be eliminated by bias reversal. Unfortunately, this excess low-frequency flux noise increases when the operation temperature is reduced below about 2 K, in contrast to the effect of critical current fluctuations that decreases with temperature [26].
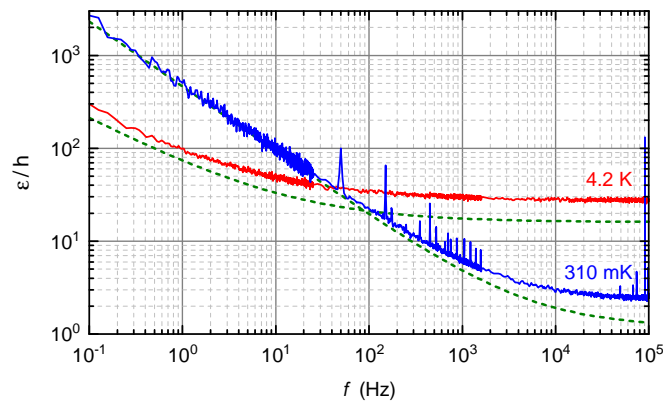
Fig. 3. Example of noise spectra for a SQUID with strongly overdamped Josephson junctions (device C214G05 in [24]). Solid lines show the measured noise at 4.2 K and 310 mK, dashed lines are calculated from Eqs. (5) and (6) for $L = 110$ pH and $R = 5.4$ Ω. The exponent α was determined from the measured noise spectra: $\alpha = 0.53$ at 4.2 K and $\alpha = 0.7$ at 310 mK, respectively. The good agreement between measured and calculated low-frequency data at 310 mK is coincidental.

A special peculiarity of the excess flux noise is a weaker scaling with frequency, $S_\Phi \propto 1/f^a$ with α typically around 0.6 for low-noise devices [24,26,27]. The increase in the noise at low temperatures is accompanied by a rise in the exponent α. Recently, the noise energy of a large variety of SQUIDs at 4.2 K and <320 mK was reported, and an approximate equation for the noise energy including low-frequency excess noise was empirically found for α ranging between about 0.5 and 0.9 [24]

$$\varepsilon \approx \varepsilon_w + 0.09h \times (f/200\,\text{kHz})^{-\alpha} \quad . \tag{6}$$

Eq. (6) gives an estimate of the excess flux noise between about 1 Hz and 100 kHz. It is applicable to SQUIDs when other sources of low-frequency noise (for example due to critical current fluctuations or picked up environmental noise) do not noticeably contribute. At very low frequencies $\lesssim 0.1$ Hz, the common $1/f$ scaling ($\alpha \approx 1$) is typically observed. The dashed lines in Fig. 3 are calculated with Eq. (6) for the experimentally observed α values of 0.53 at 4.2 K and 0.7 at 310 mK, respectively. The agreement between the calculated and measured noise spectra is adequate considering that Eqs. (5) and (6) are approximate formulas only. To conclude, the white noise decreases with temperature as expected. Cooling the SQUID to $\lesssim 300$ mK helps to improve the noise energy by typically about one order of magnitude compared to operation at 4.2 K. However, it is generally observed that the low-frequency noise degrades when lowering the temperature below about 2 K. For the particular device in Fig. 3, the noise at 310 mK exceeds that at 4.2 K for frequencies below about 40 Hz.

Therefore, operation at millikelvin temperatures is usually not favorable for low-frequency applications.

C.   Inductance and Effective Area

The basic equations for designing a SQUID sensor are summarized in chapter 5 of [4]. In this section, we present equations for calculating the inductance and the effective field-sensitive area of two representative superconducting structures. The polygonal structure in Fig. 4(a) is commonly used for thin-film pick-up coils or for the SQUID loop [28]. A narrow slit, indicated in Fig. 4(a) by a vertical solid line, interrupts the loop to enable connection with other elements, for example the two Josephson junctions. For simplicity, we first neglect the contribution of the slit to the total inductance and effective area of the polygonal loop. In practice, the slit's contribution can be made small by covering it with a superconducting plate, however, at the expense of additional stray capacitance [29]. The coplanar line in Fig. 4(b) typically serves as an interconnect line, for example between pickup coils in planar thin-film gradiometers [30], or as a "spoke" in multiloop magnetometers [20]. It has a larger parasitic inductance and effective area than the microstrip geometry (where one strip is placed on top of the other), but a substantially reduced capacitance. The latter is beneficial because stray capacitance should always be minimized in SQUID design.
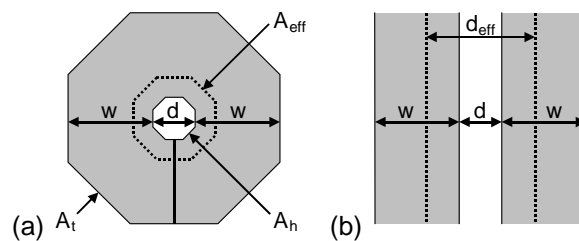
Fig. 4. Top view of two basic superconducting structures: (a) polygonal loop, (b) coplanar line. Superconducting films are marked in gray. In (a), the hole area A_h is defined by the inner perimeter of the polygonal loop and A_t is the total area (gray region plus A_h). The effective area A_{eff} and effective slit width d_{eff} are indicated by dotted lines for the depicted case $w = 2d$.

When applying a homogeneous flux density B to the superconducting loop in Fig. 4(a), magnetic flux is focused into the hole, in particular if the hole diameter d is much smaller than the linewidth w [31]. The effective area A_{eff} is defined by $A_{eff} = \Phi_h/B$ where Φ_h is the total flux focused into the hole area A_h. In other words, A_{eff} is the area that a superconducting loop with $w \to 0$ should have to collect the same total flux for given B. Similarly, flux is focused into the slit of the coplanar line in Fig. 4(b). The effective slit width d_{eff} is equal to the slit width d of an equivalent coplanar line with $w \to 0$.

Unfortunately, analytical equations for L_h and A_{eff} of the polygonal loop in Fig. 4 exist in special cases only [31]. At PTB, we are using the following approximate equations that were deduced from numerical calculations under the assumption of idealized superconducting structures (i.e., film thickness t and London penetration depth λ_L are much smaller than the linewidth w and spacing d) [32]. The equations were derived for a regular polygon with N corners, but are useful for other shapes as well (for example the optimized multiloop magnetometer in [33]). For the inductance of the polygonal loop we find

$$L_h = \gamma_L \mu_0 c/\pi \quad \text{with} \quad \gamma_L = [\ln(d/w+2.8)+0.2+2.7d/c]/2.07 \quad , \tag{7}$$

where $\mu_0 = 4\pi \times 10^{-7}$ H/m is the vacuum permeability and c is the perimeter of the hole. The inductance is proportional to the hole perimeter c multiplied by a geometry factor γ_L. This geometry factor depends on the ratio d/w, but also on the shape of the loop due to the term $2.7d/c$ in Eq. (7). For a regular polygon one obtains the perimeter

$$c = N\tan(\pi/N)d \quad . \tag{8}$$

For a square loop ($N = 4$) in the limit $d/w \to 0$, a hole inductance $L_h = 1.25\,\mu_0 d$ was numerically calculated by Jaycox and Ketchen [29] which is about 7% larger than the result $L_h = 1.17\,\mu_0 d$ obtained from Eq. (7). However, the numerical result $L_h = 1.19\,\mu_0 d$ reported in [34] is in good agreement with Eq. (7). For an octagonal loop in the limit $d/w \to 0$, a hole inductance $L_h \approx 1.05\,\mu_0 d$ was quoted in [28] which agrees well with $L_h = 1.04\,\mu_0 d$ resulting from Eqs. (7) and (8).

The effective area of the polygonal loop is given by

$$A_{\mathrm{eff}} = \gamma_A (A_h A_t)^{1/2} \quad \text{with} \quad \gamma_A = 1 - 0.68/(d/w + 2.07)^{1.75} \quad . \tag{9}$$

The geometry factor γ_A depends on the ratio d/w, but is independent of the shape of the loop. A_h and A_t are the area of the hole and the total area of the loop, respectively. For a regular polygon we obtain

$$(A_h A_t)^{1/2} = (N/4)\tan(\pi/N)d(d + 2w) \quad . \tag{10}$$

In the limiting cases of square ($N = 4$) or circular ($N \to \infty$) shapes, Eq. (10) simplifies to $(A_h A_t)^{1/2} = d(d + 2w)$ or $d(d + 2w)\pi/4$, respectively. For a circular loop, the effective area was analytically calculated in the limit $d/w \to 0$ [31]. Eq. (9) differs from the analytical result $\gamma_A = 8/\pi^2$ by less than 0.12%. For a square loop, the numerical result $\gamma_A = 0.81$ in [34] is in excellent agreement with Eq. (9). However, the experimental value $\gamma_A \approx 1.1$ reported by Ketchen *et al.* [31] is 36% higher than Eq. (9) predicts. In Ketchen's experiments, the slit had been covered by a superconducting plate. The increase in effective area was probably caused by the residual stray flux coupled into the loop via the slit.

The inductance per length L' and effective slit width (effective area per length) d_{eff} of an infinitely long coplanar line according to Fig. 4(b) can be analytically calculated, yielding $L' = \mu_0 K(k)/K(k')$ [35] and $d_{\mathrm{eff}} = 0.5\pi(d + 2w)/K(k')$. Here, $K(k)$ is the complete elliptic integral of the first kind with modulus $k = d/(d + 2w)$ and $k' = (1 - k^2)^{1/2}$. Simplified but still accurate approximate formulas without elliptic integral [32] are given here:

$$L' = \gamma_{L'}\mu_0 \qquad \text{with} \quad \gamma_{L'} = [\ln(4d/w + 22)/\ln(8w/d + 4.9)]/1.98 \quad , \tag{11}$$

$$d_{\mathrm{eff}} = \gamma_d(d + 2w) \quad \text{with} \quad \gamma_d = 0.5\pi/\ln(8w/d + e^{\pi/2}) \quad . \tag{12}$$

The term $e^{\pi/2}$ ensures that Eq. (12) yields the correct result $d_{\mathrm{eff}} \to d$ in the limit $w/d \to 0$. Neglecting the influence of the line ends, the total inductance and effective area of a coplanar line of finite length l are given by $L = L'l$ and $A_{\mathrm{eff}} = d_{\mathrm{eff}}l$, respectively.

The geometry factors according to Eqs. (7) to (12) are plotted in Fig. 5 versus the aspect ratio w/d in a wide range 10^{-3} to 10^2. Due to the ln terms in the equations, the dependence on w/d is relatively weak. For large aspect ratios $w/d \gg 1$, the geometry factors of the polygonal

loop become independent of w/d as reported in literature [29,31]. For comparison, the geometry factor $\gamma_w = 0.5\ln(8d/w) - 1$ for the inductance $L_w = \mu_0\gamma_w d$ of a circular wire-wound coil in the limit $w/d \ll 1$ is shown in Fig. 5 as dotted line [36]. In this case, w denotes the wire diameter and d the coil diameter.
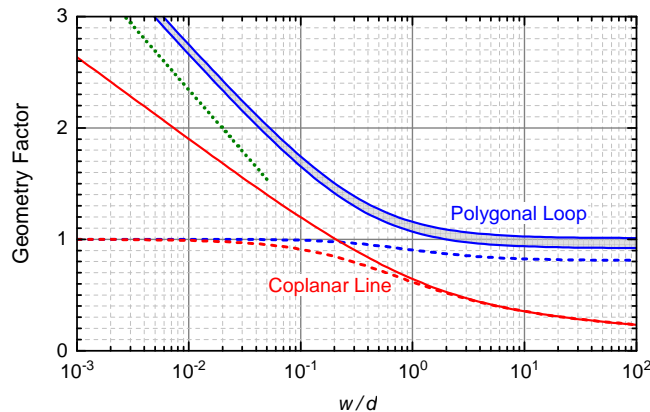
Fig. 5. Calculated geometry factors of the structures in Fig. 4 plotted versus the aspect ratio w/d. Solid lines show the inductance (γ_L and $\gamma_{L'}$), dashed lines the effective area and slit width (γ_A and γ_d). The inductance of the polygonal loop also depends on the shape due to the term $2.7d/c$ in Eq. (7); here, the two limiting cases of square ($N = 4$, lower trace) and circular ($N \rightarrow \infty$, upper trace) shape are shown, respectively. For comparison, the geometry factor of a circular wire-wound coil is indicated as dotted line [36].

The polygonal loop is commonly contacted at the outer edge, for example to the Josephson junctions or to a interconnect line. So far we have neglected the effect of the slit, i.e., we have assumed an infinitely narrow slit. A finite slit width will add parasitic inductance L_{sl} and increase the effective area by $A_{sl,eff}$. This can be estimated by approximating the slit by a piece of coplanar line and using Eqs. (11) and (12) to calculate L_{sl} and $A_{sl,eff}$. As L' and d_{eff} of the coplanar line depend only weakly on the aspect ratio w/d, the actual choice of w/d is not crucial. For example, a typical value for the inductance of a slit $L' = 300$ nH/m was quoted in [28]. This value is obtained from Eq. (11) for $w/d = 86$. Decreasing or increasing w/d by a factor of 2 changes L' by only +12% or –10%, respectively.

Finally, the presented equations can also be applied to calculate an elongated loop with $d_{long} > d_{short}$. For this, the loop is approximated by a combination of a coplanar line of length $d_{long} - d_{short}$, "capped" on both ends by half a polygonal loop with inner dimension d_{short}. The total inductance and effective area are estimated from Eqs. (7) to (12) as the sum of the contributions from coplanar line and polygonal loop. This approach is used at PTB to estimate the inductance and effective area of the SQUIDs shown as examples in the following sections.

II. MAKING THE SQUID A PRACTICAL DEVICE

A. The Bare SQUID

So far we have discussed a "bare" SQUID, i.e., a device without coupling structures that just consists of a superconducting loop with two resistively-shunted Josephson junctions as schematically shown in Fig. 1(a). Fig. 6(a) shows an implementation of such a device that was intended as a miniature magnetometer for analyzing the residual magnetic field in cryogenic setups. The SQUID loop was designed to achieve a field sensitivity of 2 µT/Φ_0 corresponding

to an effective area of 1034 μm^2. A single-turn coil on top of the loop allows one to apply a feedback current I_F to the device (this is required for operation, see section III). The mutual inductance between this coil and the SQUID loop is $M_F = 47.5$ pH, corresponding to a current sensitivity $1/M_F = 43.5$ $\mu A/\Phi_0$.
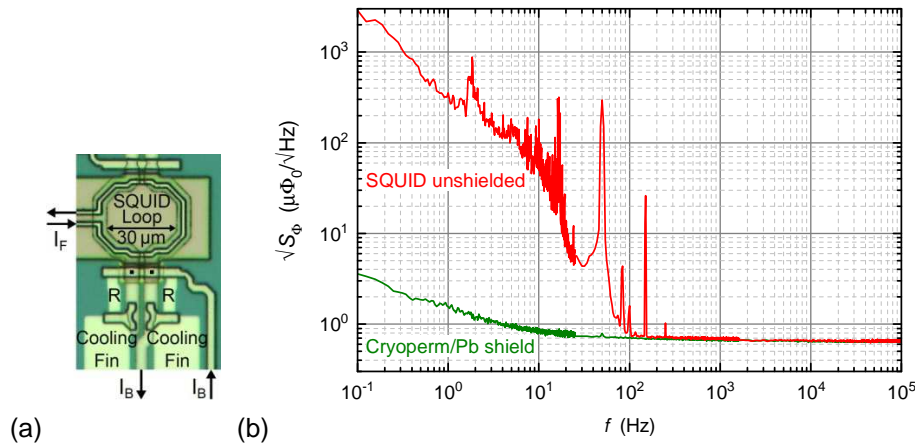
Fig. 6. (a) Micrograph and (b) flux noise spectrum of a basic SQUID with a nominal field sensitivity of 2 $\mu T/\Phi_0$ (corresponding to an effective area of 1034 μm^2). The two Josephson junctions are indicated by black squares. The noise was measured at $T = 4.2$ K with and without a superconducting shield enclosing the device. The increased noise level without shield is due to pick-up of environmental magnetic noise. The roll-off above about 10 Hz results from the screening effect of the metal liquid-helium transport dewar used for the measurement.

The lower trace in Fig. 6(b) shows the flux noise measured with a superconducting shield enclosing the device. The white noise level of 0.65 $\mu\Phi_0/\sqrt{Hz}$ corresponds to a flux density noise level of 1.3 pT/$\sqrt{Hz}$, which is just comparable to a low-noise flux-gate magnetometer. Although this noise level is achieved with a very small device (which can be advantageous in some applications) one sees that the bare SQUID is not really a sensitive magnetometer. In subsection D we will discuss how the magnetic field sensitivity of the SQUID can be improved by three to four orders of magnitude to achieve noise levels down to below 1 fT/$\sqrt{Hz}$.

Besides magnetometry, the other main application of SQUIDs is current sensing. For this, the signal current to be measured is passed through the single-turn feedback coil (now used as an input coil) and the resulting flux change in the SQUID loop is sensed via the SQUID voltage. The figure of merit for a current sensor is the current noise referred to the input coil. With the measured current sensitivity one obtains a current noise level of 28.3 pA/$\sqrt{Hz}$. This is too high for most applications. Furthermore, as shown by the upper trace in Fig. 6(b), the low-frequency noise rises by orders of magnitude when operating the SQUID without magnetic shield. This results from the SQUID's sensitivity to magnetic fields. Although being too small for magnetic field sensing applications, it is by far too high for unshielded operation in current sensing applications. In the following section we will show, how the current noise can be improved while making the device less sensitive to environmental magnetic noise. Note that in Fig. 6(b) the flux noise without shield of about 300 $\mu\Phi_0/\sqrt{Hz}$ at 1 Hz corresponds to a flux density noise of 0.6 nT/$\sqrt{Hz}$. Values around 1 nT/$\sqrt{Hz}$ at 1 Hz are quite common at the PTB site located in an urban area (Berlin). This is about six orders of magnitude larger than the intrinsic noise level of an optimized SQUID magnetometer. The peak-to-peak power-

line interference typically lies in the range of 100 nT to 1 μT.

B.   Low-Inductance Current Sensors

The noise of a SQUID-based current sensor can be reduced by connecting a large number N_S of SQUIDs in series [37]. Provided that all devices in a SQUID series array (SSA) are identical and that the signal current is equally well coupled to all of them, the SSA behaves like a single SQUID with increased output voltage. As the noise voltages across the individual SQUIDs of the array are uncorrelated, the total rms noise voltage scales with $\sqrt{N_S}$. In contrast, the voltage changes caused by the input signal add coherently and, hence, the total output voltage of the SSA increases linearly with N_S. Therefore, the signal-to-noise ratio of the SSA improves with $\sqrt{N_S}$, i.e., the effective rms flux and current noise levels scale with $1/\sqrt{N_S}$.

To make the SSA insensitive to magnetic fields, the individual SQUID loops may be configured as so-called first-order gradiometers, i.e., two equally large loops with different orientation are connected in series to get zero net flux if an homogeneous magnetic field is applied. An example of a chip containing two independent arrays of 16 SQUIDs each is depicted in Fig. 7 along with a simplified circuit diagram. The chip is an improved variant of the initial version described in [38]. First-order gradiometers are implemented as indicated by a bold black line in the magnification Fig. 7(c). Elongated SQUID loops are used to obtain a good magnetic coupling with the single-turn input and feedback coils. A total SQUID inductance $L \approx 145$ pH is estimated using the analysis described in section I C. The input inductance of the array is < 3 nH. Inductor-resistor filters between the individual SQUID cells and shunt resistors across the input coils were implemented to obtain smooth and well-behaved array characteristics, in particular at millikelvin temperatures. Integrated bias resistors R_b between nominally 0.2 mΩ and 200 mΩ are intended for the readout of superconducting detectors. The required resistor can be selected by wire-bonding to the corresponding pad. All lines to the room temperature electronics (left side of the chip) are passed through on-chip rf filters.

A critical issue for SSAs is flux trapping during cool-down. If the background flux in the individual SQUIDs differs due to the stray field of vortices trapped in the films, the voltage-flux characteristics do no longer add coherently and the overall characteristic can be severely distorted. Therefore, the linewidth in the critical parts of the array should be chosen such that vortices cannot enter the film during cool-down, and closed superconducting loops should be avoided which can trap flux due to screening currents or noise. The latter issue implies that arrays of parallel gradiometer SQUIDs [39] have strongly reduced cooling fields compared to series gradiometers and are therefore not recommended. It was shown [40] that complete vortex expulsion from narrow superconducting strips of width w occurs if the cooling field B_{cool} is kept in the range

$$B_{cool} \lesssim \Phi_0/w^2 \quad . \tag{13}$$

Thus, to reliably cool down a SQUID array in the Earth's magnetic field (≈ 50 μT) a maximum linewidth of about 5 μm should be used. For a 2.5 μm technology this means that only a single-turn input coil can be realized. Therefore, the input coils of the devices in Fig. 7 are just 2.5 μm wide lines on top of the narrow SQUID loops. The feedback lines (where the magnetic coupling needs not to be maximized) are located on both sides of SQUID the loops in a coplanar structure.
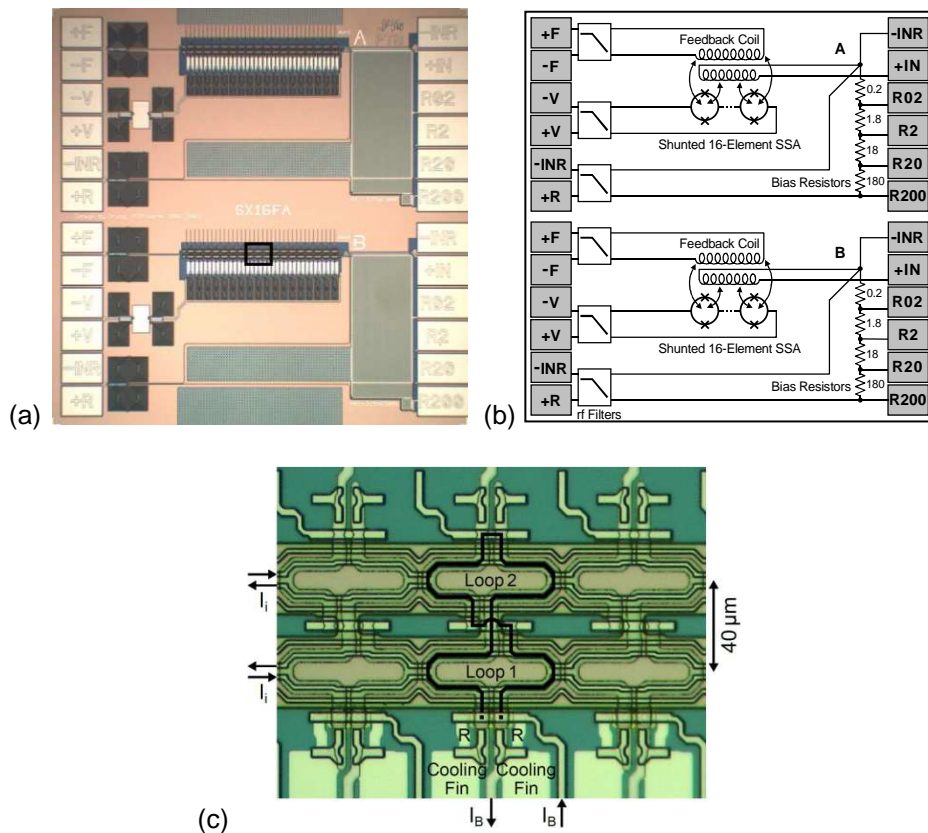
Fig. 7. (a) Micrograph and (b) simplified equivalent circuit of a sensor chip with two separate 16-element SSAs and integrated bias resistors R_b between nominally 0.2 mΩ and 200 mΩ (PTB type X16FA). The displayed area is 3 mm × 3 mm. In (b) the SQUIDs are drawn as circles with two crosses indicating the Josephson junctions, and nominal resistance values are quoted in mΩ. In (c), a magnification is shown with three individual SQUID cells. The displayed region is marked in (a) by a black frame. The SQUIDs are configured as first-order series gradiometers as indicated by a bold black line. The different colors in (a) and (c) result from the microscopes used.

In the above considerations we have assumed that for optimum performance all SQUIDs in the array should be identical. However, varying the loop size or input coil mutual inductance intentionally, one can obtain a nonperiodic transfer characteristic with a unique peak at zero flux [41-43]. These irregular arrays can be used to measure the absolute magnetic field in contrast to single SQUIDs or regular arrays that detect field changes only due to the Φ_0 periodicity in their characteristics. However, both regular and irregular SQUID arrays suffer from flux trapping which is an important issue for absolute field sensors. In this chapter, only regular arrays are discussed because they are much more common than irregular ones.

Fig. 8 shows the flux noise obtained at 4.2 K with a 32-element SSA. This device is similar to the one in Fig. 7, but involves twice the number of SQUIDs and an extra circuit to reduce the current noise contribution of the room temperature preamplifier. A low white noise level of 0.17 $\mu\Phi_0/\sqrt{Hz}$ is found, corresponding to about 1 $\mu\Phi_0/\sqrt{Hz}$ in the individual SQUIDs. This is a typical value for well-designed SQUIDs with $L \approx 145$ pH and implies a noise energy $\varepsilon \approx 22$ h. Due to the low flux noise, the input-referred current noise of about 4.5 pA/$\sqrt{Hz}$ is a factor of 6 lower than that of the bare SQUID in Fig. 6. Furthermore, the effective area is only about 1 μm^2 in all three spatial directions (in-plane and perpendicular to the chip),

corresponding to a field sensitivity of about 2 mT/Φ_0. This is a factor of 1000 improvement over the bare SQUID in Fig. 6, and leads to a substantially smaller noise degradation when operating the SSA unshielded (upper trace in Fig. 8).
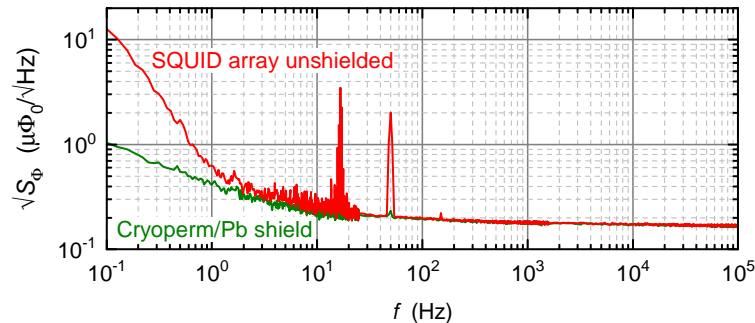
Fig. 8. Flux noise spectrum of a 32-element SSA (PTB type X216FB) measured at $T = 4.2$ K with and without a superconducting shield enclosing the device. The SSA was optimized for current sensing applications and involves on-chip current feedback to reduce the effect of preamplifier current noise (see section III C). The individual SQUIDs are of the same design as those in Fig. 7.

SSA current sensors are generally more susceptible to environmental noise pickup than single SQUIDs. This results from the fact that environmental noise (when homogeneous over the area of the SSA) is added coherently, so that the resulting total excess flux noise is identical to that of a single SQUID. In contrast, the intrinsic flux noise of the SSA improves with increasing N_S compared to a single SQUID and, hence, the signal-to-noise ratio of the SSA degrades more strongly by noise pickup.

So far we have implied the common way of SQUID operation called current bias, where a constant current is passed through the device and the voltage across it is measured. Alternatively, the SQUID can be operated with voltage bias by connecting a voltage source in parallel to the device and sensing the current change through the SQUID caused by the applied magnetic flux. For sensing this output current, the SSAs described above are well suited because they have an adequate noise level, a low magnetic field sensitivity, and zero dc input impedance due to the superconducting input coil. The voltage source can be implemented by a low-value resistor through which a current is passed. Integrating all components on a single chip, a compact two-stage sensor can be realized that has overall characteristics like a single SQUID [38]. An example of such a sensor will be shown in the following section. The SQUID bias modes and the dimensioning of a two-stage setup are discussed in detail in literature (for example in chapter 2 of [3]).

C.   High-Inductance Current Sensors

The SSAs described in the previous section are well suited for the readout of superconducting detectors or as low-noise preamplifiers in two-stage setups. However, the current noise is in the pA/√Hz range, and the input inductance is far below 1 µH. A large input inductance and a considerably increased current sensitivity can be achieved by using a multiturn input coil. Early SQUID devices in the 1960s and 1970s were equipped with wire-wound Nb coils. At around 1980, thin-film coupling schemes were introduced [29,44-46]. The most widely used scheme is depicted in Fig. 9. A SQUID loop with a large linewidth w serves a so-called "washer" onto which a spiral multiturn coil is placed. As shown in Fig. 5, the inductance of a

polygonal loop becomes independent of the aspect ratio w/d if the linewidth w is made much larger than the hole dimension d. Thus the design of the structure in Fig. 9 is relatively straight-forward: One selects the hole dimension to obtain the desired hole inductance L_h, and expands the outer dimension of the washer to accommodate the required number of turns N_i for the intended input coil inductance L_i.
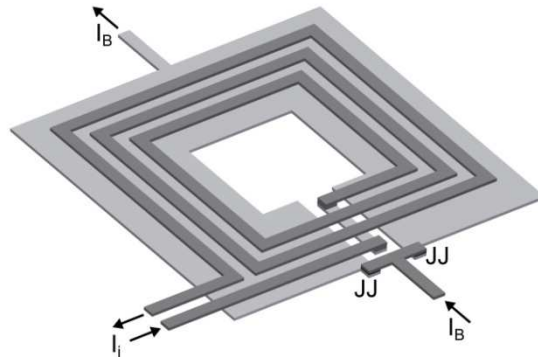
Fig. 9. Thin-film coupling scheme developed by Ketchen and Jaycox [29]. In the original design the slit was covered by a superconducting plate, requiring three superconducting layers. Here, a simplified variant with two superconducting layers is shown. An input coil with three turns is drawn; in practice, up to about 100 turns are common. The shunt resistors in parallel to the Josephson junctions (JJs) are omitted for clarity.

For typical parameters, a high coupling constant $k = M_i/(L_iL)^{1/2} \approx 0.9$ is easily achieved. Neglecting coupling losses ($k \approx 1$), the mutual inductance between input coil and SQUID M_i and the input coil inductance L_i are given by

$$M_i \approx N_iL \quad , \quad L_i \approx N_i^2L \quad . \tag{14}$$

More detailed and accurate equations are given in [29]; however, Eq. (14) is often sufficient for dimensioning the SQUID. In practice, there is not much degree of freedom in the design. Once the hole size is fixed, one can basically only adjust the number of turns for obtaining the desired input inductance.

In Fig. 9 the tunnel junctions are located at the outer edge of the washer where the magnetic fields are low. The layout involves two superconducting layers only, which is achieved by wiring the return line of the input coil through the slit. This increases the inductance contribution of the slit, but the effect on the overall performance is modest as the input coil partially couples flux into the slit, thereby increasing the mutual inductance M_i together with the total SQUID inductance L. The slit can be covered by a superconducting plate to minimize its inductance contribution, but this introduces significant parasitic capacitance and requires a third superconducting layer [29]. Generally, microwave resonances in the structure are a severe problem. They can strongly distort the SQUID characteristics and increase the noise level substantially by down-mixing. As mentioned in section I B, proper resonance damping is crucial to achieve a low noise level in practice [21-23]. Although low-noise operation was reported even without resonance damping (for example in [46]), resonance damping is strongly recommended because it makes the device more robust and tolerant against parameter variations.

To give an example, 71 turns are required according to Eq. (14) for coupling a 1 μH input inductance to a 200 pH SQUID loop. For a conventional fabrication process with 2.5 μm

minimum linewidth and spacing, a 5 μm pitch in the spiral input coil and a total width $w \approx$ 355 μm are obtained. Assuming $L' \approx 0.3$ pH/μm for the slit [28], the total contribution to the SQUID inductance $L_{sl} \approx 107$ pH is about half the intended SQUID inductance. This example shows that with a 2.5 μm fabrication technology, the SQUID inductance cannot be lowered below about 100 pH when using the design in Fig. 9. As mentioned above, the slit could be covered, but this increases the parasitic capacitance and requires an extra superconducting layer. The increase in capacitance can easily undermine the benefit of a reduced SQUID inductance. When connecting several washers in parallel (typically two or four) and their input coils in series, the total SQUID inductance is reduced and the total input inductance increases [28,47]. This relaxes the problem of large inductance ratios L_i/L. Gradiometric configurations with multiple washers are beneficial to reduce the sensitivity to external magnetic fields.

An elegant way to couple a large input inductance to a small SQUID inductance is to use an extra input transformer [23,38,48]. In the double-transformer scheme, the spiral coil on top of the SQUID washer is connected to the secondary (low-inductance) side of the input transformer, whose primary (high-inductance) side is used for the input coil. Typically, the input transformer is designed in the same way as the SQUID transformer, i.e., its low-inductance side acts as a "washer" for the multiturn input coil. Without coupling losses in the two individual transformers, the overall coupling is also ideal, $k = 1$. However, for finite coupling losses in the transformers, the overall coupling degrades relatively strongly. Unfortunately, the equations for the overall coupling constant are somewhat cumbersome. Assuming for simplicity that both transformers have the same coupling constant k_0 and that the inductance of the spiral coil on the SQUID washer is equal to the low-inductance side of the input transformer, the overall coupling constant is given by $k = k_0^2/(2-k_0^2)$ [38]. Thus, for relatively high individual coupling constants k_0 of 90% or 80% the overall coupling constant k degrades to 68% or 47%, respectively. On the other hand, in the double transformer scheme the transformers require fewer turns, leading to reduced parasitic capacitance. The degradation in coupling is (partially) compensated by smooth, well-behaved SQUID characteristics and a low noise level.

An example of a practical SQUID with double-transformer coupling is shown in Fig. 10. It is an improved version of the device described in [38], and was fabricated using a Nb-AlOx-Nb trilayer process with two superconducting layers and a minimum lithographic feature size of 2.5 μm. It has a high input inductance $L_i \approx 1.8$ μH which is coupled to the SQUID inductance $L \approx 80$ pH with an overall coupling constant $k \approx 0.72$. Two large input transformers (each with a 40-turn input coil shunted by a resistor-capacitor series circuit) are wired as a first-order series gradiometer in order to reduce the sensitivity to homogeneous magnetic fields. Variants with fewer turns (down to 4 on each input transformer) were also implemented to cover the input inductance range down to about 24 nH. An additional feedback transformer in series to the input coil is intended for applications where the feedback current is applied to the input circuit (nulling the input current minimizes crosstalk in multichannel magnetometer systems [49]).

To protect the input against large currents in magnetic resonance experiments, an optional on-chip current limiter (Q spoiler [50]) may be used. It is realized in Fig. 10 by a series array of 16 unshunted 20 pH SQUIDs connected in series to the input coil. All lines connecting the sensor chip with the room temperature readout electronics are passed through on-chip rf filters. The SQUID is designed with four parallel loops, arranged as a second-order gradiometer. A 16-element SSA is integrated on the chip to act as a low-noise preamplifier.

Current feedback between the SQUID sensor and the SSA is utilized to increase the overall gain (see section III C). A typical white flux noise of $0.8\,\mu\Phi_0/\sqrt{Hz}$ is achieved at 4.2 K, resulting in a current noise level (referred to the input coil) of ≈ 0.2 pA/$\sqrt{Hz}$ for the nominal current sensitivity $1/M_i = 0.24\,\mu A/\Phi_0$. At $\lesssim 300$ mK, the white noise typically drops to $0.25\,\mu\Phi_0/\sqrt{Hz}$.
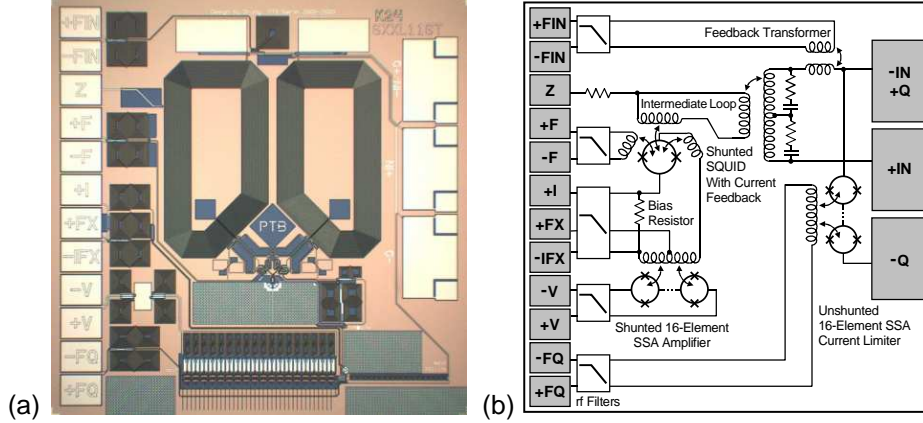
Fig. 10. (a) Micrograph and (b) simplified equivalent circuit of a current sensor with an input inductance of about 1.8 µH (PTB type XXL116T). The integrated two-stage sensor involves double-transformer coupling and is equipped with an optional input current limiter [38]. The displayed area is 3 mm × 3 mm.

An important figure of merit for superconducting current sensors is the coupled noise energy ε_c referred to the input inductance L_i rather than to the SQUID inductance L. Using the current noise density referred to the input coil $S_I = S_\Phi/M_i^2$ one obtains

$$\varepsilon_c = S_I L_i/2 = S_\Phi/(2k^2 L) = \varepsilon/k^2 \quad . \tag{15}$$

The input-referred noise energy ε_c of the device in Fig. 10 is typically 50 h at 4.2 K and 5 h at $\lesssim 300$ mK, respectively. Note that at 4.2 K single-stage sensors (devices without the SSA preamplifier) achieve nearly the same noise level; however, when operating a current sensor at millikelvin temperatures, a two-stage readout is required to avoid the noise being dominated by the room-temperature readout electronics (see section III).

D.   *Magnetic Field Sensors*

The "traditional" way of realizing a sensitive magnetic field sensor is to connect a superconducting wire-wound pickup coil to the input coil of a SQUID current sensor. This scheme was introduced soon after the invention of the SQUID and is still widely used. Fig. 11 shows two examples, a magnetometer and a first-order gradiometer. In the case of a magnetometer, the magnetic flux in the pickup coil, $\Phi_P = BA_P$, causes a screening current $\Phi_P/(L_P+L_i)$ which flows through the input coil, thereby generating a change in the magnetic flux Φ in the SQUID. The flux transfer coefficient is

$$\Phi/\Phi_P = M_i/(L_P+L_i) \approx 0.5\,k(L/L_P)^{1/2} \quad . \tag{16}$$

For the optimization we assume that for given SQUID inductance L the input coil inductance L_i is varied by the number of input coil turns N_i while the coupling constant $k = M_i/(L_i L)^{1/2}$ remains constant. Under this condition, the flux transfer Φ/Φ_P is maximized for matched inductances $L_i = L_P$. The approximation on the right side of Eq. (16) is obtained for the optimum case $L_i \approx L_P$. Note that in practice it is not very crucial to exactly keep the matching condition because the optimum is quite wide. Being a factor of two away from optimum ($L_i/L_P = 0.5$ or 2), reduces the flux transfer by 5.7% only. Furthermore, when considering the resulting field noise, one has to include the fact that the effective SQUID inductance is reduced in the presence of the pickup coil by screening effects. The detailed optimization is rather complicated [23]. Fortunately, in practice the straight-forward condition $L_i \approx L_P$ is generally sufficient for dimensioning a magnetometer.
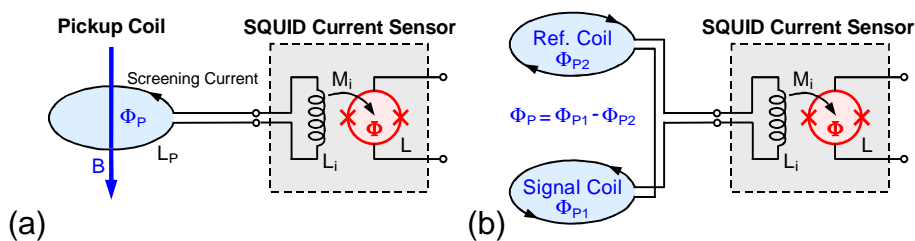
Fig. 11. Coupling a wire-wound pickup coil to a SQUID current sensor: (a) Magnetometer and (b) axial first-order gradiometer.

Knowing the flux transfer coefficient, the effective area of the magnetometer $A_{eff} = A_P \times \Phi/\Phi_P$ can be calculated from the pickup coil area A_p. The resulting noise is given by

$$S_B = S_\Phi/A_{eff}^2 \approx \varepsilon_c\, 8 L_P/A_P^2 \quad . \tag{17}$$

The approximation on the right side is valid for the matched case $L_i \approx L_P$. For fixed pickup coil parameters L_P and A_P, the noise scales with the coupled noise energy ε_c. The self inductance of the wire-wound pickup coil can be calculated with the approximation $\mu_0 d_P [0.5 \ln(8 d_P/w_P) - 1]$ given in [36] (d_P and w_P are the diameters of the coil and the wire, respectively). The inductance contribution of the interconnect lines between pickup coil and SQUID can be included in the total pickup coil inductance L_P. Assuming for example a circular single-turn pickup coil with 20 mm coil diameter, 0.1 mm wire diameter, and a 16 cm twisted pair with $L' = 4$ nH/cm between pickup coil and SQUID, the total pickup coil inductance amounts to 132 nH. Coupling this to a SQUID with $\varepsilon_c \approx 50\, h$ will result in a noise level $\sqrt{S_B} \approx 0.6$ fT/$\sqrt{\text{Hz}}$ according to Eq. (17). In this example, the dimensioning was sub-optimal because the contribution of the twisted pair was relatively high (about a quarter of the total inductance $L_P + L_i$). Using a multiturn pickup coil and a correspondingly increased input coil inductance would reduce the noise even further. Thus we conclude that with modern dc SQUIDs it is relatively straight-forward to achieve noise levels well below 1 fT/$\sqrt{\text{Hz}}$. In practice, the system noise level is usually limited by thermal noise currents in the superinsulation of the dewar containing the magnetometer.

Magnetometers are useful in extremely well shielded environments only. With moderate shielding, the effect of environmental interference can be reduced by wiring two identical pickup coils to a first-order gradiometer as shown in Fig. 11(b). The source to be measured (for example the human brain or heart) is located as close as possible to one of the coils, the

signal coil. Due to the strong decrease of the source's magnetic field with distance, the other coil (the reference coil) will "see" only a weak signal, i.e., the net flux will be only slightly reduced compared to a magnetometer. In contrast, the effect of a homogeneous magnetic field is suppressed because the flux contributions Φ_{P1} and Φ_{P2} in the two pickup coils cancel each other out. Thus a gradiometer strongly reduces the effect of remote noise sources that have small spatial derivatives compared to those of the local signal source. The SQUID itself is commonly housed in a well shielded package, sufficiently far away from the pickup coils to avoid distortion of the magnetic fields. An example of a practical realization is given in Fig. 12. The remote location of the SQUID package is beneficial in applications where the object under investigation is exposed to large magnetic fields that would distort the SQUID function (for example in magnetic resonance experiments).

Fig. 12. Example of a commercial SQUID package. The superconducting connection to the input coil is realized via screw contacts. For low-noise operation, the SQUID carrier is enclosed by a Nb shield. On the left side, the socket for the wiring to the room temperature electronics is visible (courtesy of Magnicon GmbH, Hamburg).

First-order gradiometers are often adequate in moderate magnetic shielding (for example a chamber with two layers of high-permeability material plus one eddy-current screen of Al). Higher order gradiometers (second or third) are required for magnetically unshielded measurements. Generally, an "ideal" gradiometer of n-th order is sensitive to the n-th and higher spatial derivatives of the applied field, but suppresses all lower spatial derivatives including the homogeneous field component. In practice, imbalance occurs due to slightly different coil areas or tilt angles, so that a "real" gradiometer is also sensitive to the homogeneous field component in all three spatial directions. In multichannel systems, the imbalance can be compensated by adding a set of reference channels (magnetometers and lower-order gradiometers).

Gradiometers cannot only be realized "in hardware" as depicted in Fig. 11, but also electronically by combining the analog outputs of different channels [51] or "in software" after digitizing the output signals of the SQUID readout electronics. The latter approach is very powerful and efficient, and typically used in large biomagnetic multichannel systems. Considering the dynamic range of the associated electronics, a suitable combination of passive and active methods (i.e., shielded room and gradiometric configurations) yields the best overall performance and can suppress environmental interference by about five orders of magnitude. A comprehensive review of shielding and noise cancellation issues with the focus on biomagnetic applications is found in chapter 3 of [3].

The wire-wound pickup coil can be substituted by a thin-film coil in order to get a compact single-chip magnetometer or gradiometer. For integrated devices, the sensitivity can be maximized by applying the multiloop concept rather than the transformer coupling of Fig. 9.

The basic idea is quite simple: the SQUID loop is directly used for collecting flux, but a large number of loops is connected in parallel to reduce the effective SQUID inductance to an acceptable level. The effective area of the complete device is given by the area of the individual loops. A theoretical description and several device examples are given in [20]. The approach of fractional-turn loops was first implemented in bulk Nb SQUIDs in the early 1970s [52]. It was later attempted as an alternative to the washer structure [45], but has not become established for SQUID current sensors. In the early 1990s, the concept was successfully applied to thin-film magnetometers [53]. A few years later, record noise levels of 1.13 fT/√Hz were obtained with a device implemented on a 7.2 mm × 7.2 mm chip [33]. The lowest noise reported so far is 0.33 fT/√Hz for a 12.5 mm × 12.5 mm device involving sub-micrometer cross-type tunnel junctions [54].
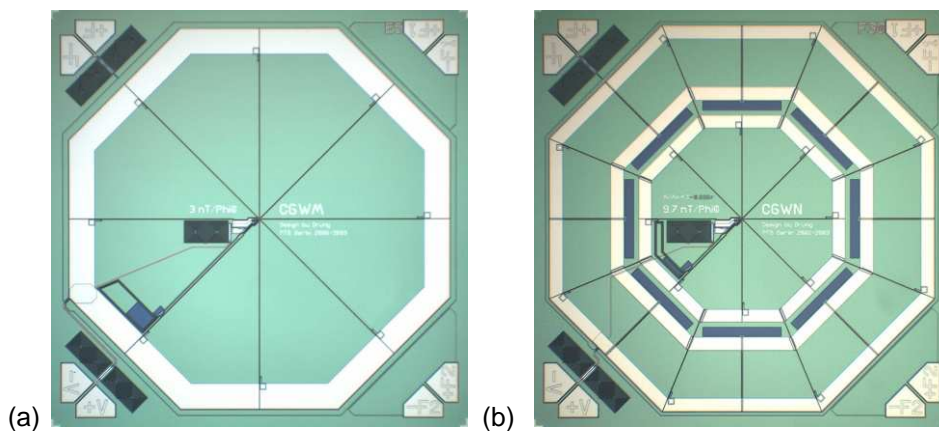
Fig. 13. Examples of integrated multiloop devices. (a) Magnetometer (PTB type WM) with a field sensitivity of 3 nT/Φ_0, (b) concentric gradiometer (PTB type WN) intended for noise thermometry. The displayed area is 3 mm × 3 mm.

Fig. 13 shows two examples of multiloop SQUIDs, a magnetometer and a concentric gradiometer. The magnetometer uses eight parallel-connected loops, yielding an effective SQUID inductance of about 120 pH. In spite of its small size (2.8 mm outer dimension, 6.5 mm^2 area), the device achieves an effective area of 0.69 mm^2 corresponding to a field sensitivity of 3 nT/Φ_0. The typical white noise level is 3 fT/√Hz. The gradiometer in Fig. 13(b) was optimized for noise thermometry. It involves a total of 8 inner loops and 16 outer loops. Each inner loop is connected in series with two parallel-connected outer loops. The resulting eight coil combinations are connected in parallel, resulting in a low effective SQUID inductance of about 130 pH. The nominal field sensitivity of the inner loops is 9.7 nT/Φ_0.

III.   SQUID READOUT

In this section, we describe the two most common concepts for operating a SQUID, flux modulation and direct readout. Digital SQUIDs are not discussed because they are rarely used in practice. Bias current reversal schemes for the suppression of critical current fluctuations are also omitted because modern Nb-AlOx-Nb tunnel junctions typically do not require them. Other types of all-refractory junctions may show large levels of excess low-frequency noise from critical current fluctuations, for example NbN junctions with MgO barrier [55] or Nb

junctions with barriers from amorphous silicon [56] or HfTi [57]. SQUIDs involving these junctions often require bias reversal schemes for low-frequency applications. Also, high-T_c SQUIDs are almost always operated with bias current reversal. Detailed reviews on SQUID readout including the various bias reversal schemes are found in literature [4,58].

A.   Flux-Locked Loop Basics

In principle, a SQUID can be operated in a small-signal mode around the optimum working point W which is typically located near the steepest part of the V-Φ characteristic (the inflection point). As illustrated in Fig. 14(a), a small change in the applied flux $\delta\Phi$ will produce a proportional change in the voltage $\delta V = V_\Phi \delta\Phi$ ($V_\Phi = \partial V/\partial\Phi$ is the transfer coefficient at the working point). However, the proportionality between voltage and flux is maintained only for very small $\delta\Phi$, and the output becomes strongly distorted if the applied flux exceeds the linear flux range Φ_{lin} which is typically a few percents of a flux quantum only. As SQUIDs are commonly applied to measure weak signals, this small dynamic range might just be sufficient. However, in practice there are usually much larger disturbing signals (for example the 50 Hz or 60 Hz power line interference) superimposed to the measurement signal, which makes a small-signal readout usually impossible unless the SQUID is very well shielded. Further disadvantages of the small-signal readout are that the transfer coefficient V_Φ depends on the bias settings of the SQUID, and that the SQUID noise increases if the applied flux shifts the working point too far away from optimum.
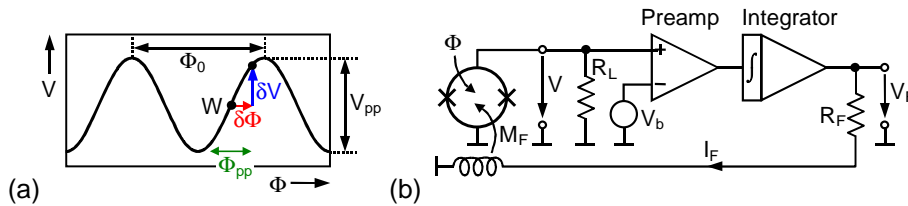
Fig. 14. Fundamentals of SQUID readout: (a) V-Φ characteristic and (b) basic flux-locked loop (FLL) circuit. The SQUID is drawn as a circle with two crosses indicating the resistively-shunted Josephson junctions, and the bias current source is omitted for clarity.

The dynamic range can be considerably increased by negative feedback. The basic circuit of the so-called flux-locked loop (FLL) is depicted in Fig. 14(b). The SQUID is biased at the working point W as in the small-signal readout. The deviation of the SQUID voltage V from that at the working point V_b is amplified, integrated, and fed back into the SQUID via a feedback resistor R_F and a feedback coil that is magnetically coupled to the SQUID via a mutual inductance M_F. Commonly, feedback resistances in the kΩ range are used, making the impedance of the feedback coil negligible in the frequency range of interest. For infinite integrator gain, the flux in the SQUID is kept constant by the negative feedback and the voltage V_F across the feedback resistor depends linearly on the applied flux. In this case, the transfer coefficient of the flux-locked SQUID

$$G_{FLL} = \partial V_F/\partial\Phi = -R_F/M_F \tag{18}$$

becomes independent of the working point. The noise does not degrade with applied flux

because the SQUID is always kept at the chosen working point. However, the integrator gain decreases with frequency, and deviations occur at high frequencies due to the reduced open-loop gain G_{OL}. For the analysis of the FLL dynamics we assume the most common case of an integrator with a single pole in the frequency response (other types of integrators are described in [3,4]). In this case, the room temperature electronics (preamplifier plus integrator) has an overall gain $|\partial V_F/\partial V| = f_{GBW}/f$ and is fully characterized by the gain-bandwidth product f_{GBW}. The SQUID can be considered as a current-to-voltage converter with a transresistance

$$A_{TR} = \partial V/\partial I_F = V_\Phi M_F/(1+R_{dyn}/R_L) \quad , \tag{19}$$

where R_{dyn} is the dynamic resistance of the SQUID at the working point and R_L is the input resistance of the readout electronics. Often the term in parentheses can be neglected because $R_{dyn} \ll R_L$. For wideband systems, however, the transmission lines between the SQUID and the room temperature amplifier should be terminated (or at least be resistively shunted). The electronics in [59] has $R_L = 50\ \Omega$ (realized by negative feedback for minimum noise) which is comparable to the R_{dyn} of PTB's 16-element SSAs. In this case, the complete Eq. (19) has to be used.

To analyze the FLL dynamics, we first assume that the feedback loop is opened (for example by disconnecting the feedback resistor from the integrator output). Knowing A_{TR}, the overall gain of the open feedback loop can be calculated as

$$|G_{OL}| = f_1/f \quad \text{with} \quad f_1 = f_{GBW}A_{TR}/R_F \quad . \tag{20}$$

The open-loop gain $|G_{OL}|$ scales inversely proportional to frequency. It falls to unity at the unity-gain frequency f_1. Now we assume that the feedback loop is closed to obtain FLL operation. The idealized FLL in Fig. 14(b) exhibits a first-order low-pass response with a 3 dB bandwidth $f_{3dB} = f_1$. The 3 dB bandwidth is the frequency at which the amplitude falls to $1/\sqrt{2}$ or –3 dB. Note that Eq. (20) was derived for the common case of a current-biased SQUID. With voltage bias, a similar analysis can be performed by describing the SQUID as a current-to-current converter and the feedback electronics as a current-to-voltage converter with a transresistance proportional to $1/f$. The expression for f_1 will differ from Eq. (20), but once f_1 is fixed, the dynamic behavior of the FLL is given independent of the way the SQUID is biased. Furthermore, the noise is generally not influenced by the SQUID bias mode. Therefore, all considerations hereinafter will apply for both bias modes.

In the basic FLL circuit in Fig. 14(b), the 3 dB bandwidth can be made arbitrarily large by increasing f_1. In practice, however, an upper limit is imposed by phase lag in the transmission lines and the readout electronics. A simple but efficient model describes the combined parasitic effects in the FLL by an effective dead time t_d [3,4]. It was shown that with finite dead time the unity-gain frequency is limited to

$$f_{1,max} = 0.08/t_d \approx f_{3dB,max}/2.25 \quad . \tag{21}$$

For larger values of f_1, the FLL exhibits a peak in the frequency response or even becomes unstable (oscillation at $\approx 0.25/t_d$). According to Eq. (21), the maximum FLL bandwidth $f_{3dB,max}$ is a factor of 2.25 larger than $f_{1,max}$. A relative increase in $f_{3dB,max}/f_{1,max}$ of up to a factor of 3 is common for wideband systems with feedback (not only for SQUIDs). Note that f_1 determines the open-loop gain and hence the linearization effect, not the FLL bandwidth f_{3B}.

Unfortunately, commonly f_{3B} is quoted rather than f_1 which gives a too optimistic view of the dynamic performance. For example, if one likes to have an open-loop gain of > 4, the highest signal frequency would be $f_1/4 = f_{3dB}/9$. Thus, in this example the maximum signal frequency is about one order of magnitude smaller than the FLL bandwidth f_{3dB}. Generally, for signal frequencies close to f_{3dB}, FLL operation is not recommended because the feedback loop does not reduce the nonlinear distortion due to phase lag, but rather increases it. In such cases, the high-frequency signal of interest is preferably measured in a small-signal readout, and a "slow" FLL could be used to suppress environmental interference at frequencies much below that of the signal.

For a typical separation of 1 m between SQUID and room temperature electronics, the dead time in the cables amounts to $t_d \approx 10$ ns. The resulting limits according to Eq. (21) are $f_{1,max} \approx 8$ MHz and $f_{3dB,max} \approx 18$ MHz, respectively. State-of-the-art readout electronics allow FLL dynamics close to these limits [59]. In 2006, a prototype FLL with SiGe transistors was operated in liquid helium nearby a 16-element SSA [38]. Due to the short distance and the wideband setup, a very small dead time $t_d \approx 0.65$ ns was achieved. The measured small-signal bandwidth of 350 MHz was even higher than $f_{3dB,max} \approx 280$ MHz predicted from Eq. (21), suggesting that the ratio $f_{3dB,max}/f_{1,max}$ was probably about 2.8 instead of 2.25. Two years later, the cold semiconductor feedback loop was substituted by a large series-parallel array of 640 SQUIDs acting as a current amplifier [60]. A low-frequency open-loop gain of about 20 and a unity-gain frequency $f_1 > 200$ MHz were reported. In both experiments, coaxial lines between 4.2 K and room temperature were mandatory. Although these experiments clearly confirm the dead time model, such high bandwidth is commonly not needed. In most cases, the commercial variant of the electronics in [59] provides sufficient bandwidth ($f_{3dB,max} \approx 20$ MHz), even when connecting the SQUID to the readout electronics via 1 m long twisted wires.

In the above discussion it was implied that f_{GBW} can be selected sufficiently high to reach $f_{3dB,max}$. For wideband systems, very high values of f_{GBW} may be required depending on the SQUID. For example, the electronics in [59] allows one to select f_{GBW} up to 7.2 GHz. The full bandwidth can be achieved at acceptable feedback resistances in the range of 10 kΩ even for SQUIDs with a small A_{TR}. Decreasing the feedback resistance to boost the bandwidth lowers the output signal amplitude and increases the demands on the data acquisition system following the analog output of the FLL.

Another important parameter is the slew rate, i.e., the maximum temporal change in the feedback flux $|\partial\Phi_F/\partial t|_{max}$. In practice, the slew rate is often more critical than the bandwidth of the FLL. It is commonly measured by applying a sinusoidal signal flux and increasing the amplitude until the FLL becomes unstable or the output saturates. Here, we discuss the slew rate at high signal frequencies, i.e., in the regime where it is not limited by the static feedback range. For the basic FLL with one-pole integrator one obtains

$$\dot{\Phi}_{F,max} = \pi\Phi_{pp}f_1 \lesssim \Phi_0 f_1 \quad \text{with} \quad \Phi_{pp} = V_{pp}/|V_\Phi| \lesssim \Phi_0/\pi \quad . \tag{22}$$

The maximum slew rate with one-pole integrator is frequency-independent. It is proportional to the unity-gain frequency f_1 and the peak-peak flux Φ_{pp} calculated from the peak-peak voltage V_{pp} according to the right side of Eq. (22). One sees that a high slew rate requires a high intrinsic linearity. For a sinusoidal V-Φ characteristic (which is often a useful first approximation) one obtains the practical upper limit $\Phi_{pp} = \Phi_0/\pi$ and a resulting slew rate

$\Phi_0 f_1$, i.e., in the best case one obtains about 1 Φ_0/μs per megahertz of bandwidth. Note that the usable linear range Φ_{lin} for the small-signal readout is much smaller than Φ_{pp} defining the "intrinsic linearity" for calculating the slew rate. Driving a SQUID to $\pm\Phi_{\text{pp}}$ would cause very high dynamic distortions. In fact, the error flux in the SQUID becomes large when approaching the slew rate limit, but the net effect with feedback is strongly reduced if the open-loop gain is high at the chosen signal frequency. The sinusoidal characteristic depicted in Fig. 14 has symmetric voltage swings $\pm V_{\text{pp}}/2$ around the working point W. For asymmetric characteristics, V_{pp} in Eq. (22) has to be replaced by twice the smaller voltage swing.

Beside linearization of the transfer function, another important task of the readout electronics is to amplify the weak signal from the SQUID without adding (too much) noise. The preamplifier in the readout electronics is characterized by a noise voltage $V_{\text{N,amp}}$ and a noise current $I_{\text{N,amp}}$ at its input. The corresponding power spectral densities are $S_{V,\text{amp}}$ and $S_{I,\text{amp}}$, respectively. It is commonly assumed that voltage noise and current noise are uncorrelated, which is not exactly true but a reasonable assumption to simplify noise analysis. The amplifier's noise voltage is superimposed to the measured SQUID voltage which increases the total noise. The amplifier's noise current flows through the SQUID, thereby generating a voltage drop via the dynamic resistance R_{dyn} of the SQUID at its working point. To describe the effect of preamplifier current noise, it is often convenient to use the current sensitivity

$$M_{\text{dyn}} = R_{\text{dyn}}/V_\Phi \approx \pm(1...2)L \quad . \tag{23}$$

M_{dyn} depends less strongly on the working point and on parasitic effects in the SQUID (for example due to resonances in the input coil) than R_{dyn}. Roughly speaking, M_{dyn} scales with the SQUID inductance L. One obtains values of $|M_{\text{dyn}}|$ between L and $2L$ for low-T_c SQUIDs covering a wide range of SQUID inductances between 7 pH and 400 pH [3]. The total noise of the SQUID including preamplifier noise is given by

$$S_{\Phi,\text{t}} = S_\Phi + S_{V,\text{amp}}/V_\Phi^2 + S_{I,\text{amp}}M_{\text{dyn}}^2 \quad . \tag{24}$$

In Eq. (24) the effect of amplifier voltage and current noise is expressed as effective flux noise contributions via V_Φ and M_{dyn}. It is is convenient to measure V_Φ and M_{dyn} in the FLL mode by superimposing small test signals to the SQUID bias voltage and current, respectively, and calculating the resulting flux change from the FLL output voltage change. This way, V_Φ and M_{dyn} are determined under the conditions of the noise measurement (that is always performed in the FLL mode) and the preamplifier noise contributions can be accurately determined. The transfer coefficients V_Φ and M_{dyn} are also applicable to more complex circuits, for example a two-stage SQUID setup. In practice, one considers the SQUID as a "black box" and measures V_Φ and M_{dyn} without regarding the actual type of circuit.

From Eq. (24) the requirements for the preamplifier can be deduced. Assuming a typical Nb-based SQUID at 4.2 K with $V_\Phi = 100\,\mu$V/Φ_0 and $1/M_{\text{dyn}} = 10\,\mu$A/$\Phi_0$, the preamplifier voltage and current noise levels should be < 0.1 nV/$\sqrt{\text{Hz}}$ and < 10 pA/$\sqrt{\text{Hz}}$ for keeping the amplifier contributions below the typical SQUID noise of 1 $\mu\Phi_0/\sqrt{\text{Hz}}$. The current noise requirement is easily met, but the amplifier's voltage noise is a severe issue. For arrays with N_S SQUIDs in series, the flux noise density S_Φ of the SSA scales with $1/N_S$, V_Φ is proportional to N_S and M_{dyn} is independent of N_S. As a result, the amplifier voltage noise term in Eq. (24)

falls with N_S^2 but the current noise term remains constant and becomes the limiting contribution to $S_{\Phi,t}$ for large value of N_S. We see that amplifier noise can substantially degrade the overall noise performance. In the following sections we will describe the two most common methods to minimze the amplifier's noise contribution.

B.   Flux Modulation Readout

Amplifier noise effects are conveniently discussed on the basis of the noise temperature [58]. For a resistive source, the total effect of amplifier noise is converted into an equivalent increase in the source resistor's temperature. For given voltage and current noise levels, the amplifier noise temperature depends on the source resistance. It has a minimum T_{min} for an optimum source resistance R_{opt} for which the contributions from amplifier voltage and current noise are equal: $R_{opt} = (S_{V,Amp}/S_{I,amp})^{1/2}$. For lowest noise, the amplifier should be designed such that R_{opt} is matched to the dynamic resistance of the SQUID R_{dyn}. The resulting amplifier noise temperature should be sufficiently low compared to the noise temperature of the SQUID, which is about four times its operation temperature according to simulations [13,14].

The achievable T_{min} and R_{opt} depend of the type of transistors used in the input stage of the amplifier. Bipolar transistors allow low values $R_{opt} \approx 50\ \Omega$, but have a relatively a high T_{min} between about 30 K and 100 K (about 200 K are possible for $R_{opt} \approx 10\ \Omega$). These noise temperatures are acceptable for the readout of high-T_c SQUIDs, but for low-T_c SQUIDs special measures have to be adopted to boost the SQUID output (section III C). In contrast, amplifiers based on junction-field effect transistors (JFETs) allow very low noise temperatures down to $T_{min} \approx 1$ K at source resistances above about 1 kΩ. Therefore, the noise of JFET-based amplifiers is sufficiently low for SQUID readout, but there is a large mismatch between R_{opt} and typical values of R_{dyn}.
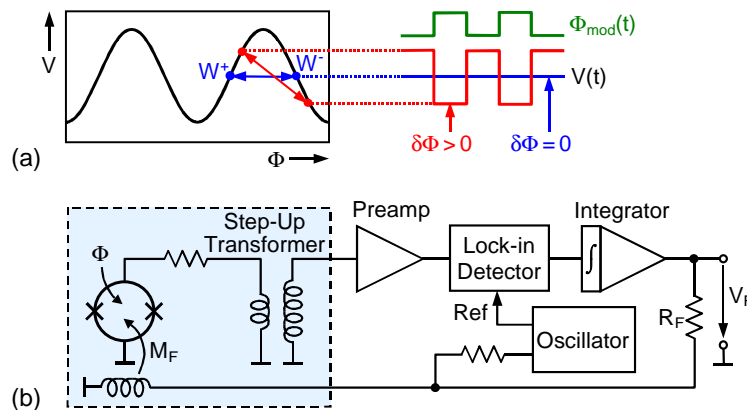
Fig. 15. SQUID readout with flux modulation: (a) V-Φ characteristic and (b) FLL circuit. A square-wave modulation flux Φ_{mod} toggles the SQUID periodically between working points W$^+$ and W$^-$ with positive and negative transfer coefficient V_Φ. Components inside the dashed box are at cryogenic temperature. The dc source for biasing the SQUID is omitted for clarity.

The straight-forward method for impedance matching is the utilization of a cold transformer in a flux-modulated readout scheme [61,62]. As shown in Fig. 15, a square-wave modulation flux $\Phi_{mod}(t)$ is applied to the SQUID to toggle between two working points W$^+$ and W$^-$ placed at adjacent slopes of the V-Φ characteristic. Without applied flux ($\delta\Phi = 0$), zero voltage across the SQUID is obtained. Applying a positive flux $\delta\Phi > 0$ results in a

square-wave SQUID voltage $V(t)$ which is out-of-phase to the modulation flux $\Phi_{mod}(t)$ as illustrated in Fig. 15(a). Accordingly, a negative flux $\delta\Phi < 0$ leads to a SQUID voltage in phase with the modulation flux. Thus, the applied flux can be sensed by synchronously detecting the SQUID voltage at the modulation frequency. This is commonly done with a synchronous switch (or a mixer in the case of wideband systems) after amplifying the SQUID output with a cold transformer followed by the room temperature preamplifier. The output of the lock-in detector is integrated and send back as a current into a feedback coil in order to counterbalance the flux applied to the SQUID. As for the basic FLL circuit in Fig. 14, the output voltage V_F represents the linearized output signal.

The resistance "seen" by the room temperature amplifier increases with the square of the transformer's turn ratio. For a suitably chosen turn ratio, the low SQUID impedance is noise-matched to the amplifier, resulting in minimum overall noise. A small resistance may be placed between the SQUID and the transformer primary to avoid that the SQUID is shorted by the transformer (the SQUID is operated with voltage bias rather than current bias).

The flux-modulation technique was introduced soon after the invention of the SQUID [61] and was the only practical readout method until the early 1990s when direct readout schemes emerged. The cylindrical dc SQUID of Clarke *et al.* [62] (which was a first milestone in the development of reliable thin-film devices) involved a cold inductor-capacitor resonant circuit. However, this is presently uncommon due to the reduced bandwidth compared to transformer coupling. Flux-modulation is an efficient way to read out SQUIDs with smooth, well-behaved V-Φ characteristics. In practice, the noise might increase if the characteristics are strongly asymmetric due to parasitic resonances in the input coil structure. Typical modulation frequencies range between 100 kHz and 500 kHz where FET amplifiers have excellent noise performance. At higher frequencies, the current noise rises due to parasitic capacitance in the transistors, and the noise temperature correspondingly degrades. Square-wave modulation is ideal in terms of noise because the SQUID is always biased at points with best noise. However, in particular at high modulation frequencies, switching spikes can increase the noise due to down-mixing. Sinusoidal modulation circumvents these problems but increases the noise because the SQUID dynamically passes through points with reduced and even no sensitivity.

The main restriction of flux-modulation readout is a limited FLL bandwidth. Obviously, the maximum FLL bandwidth is lower than the modulation frequency, which also results in a reduced slew rate. Early systems used modulation at 100 kHz. In 1984, a first wideband system with 500 kHz square-wave modulation was reported involving two transformers (one cooled and the other at room temperature) [63]. In the mid 1990s, wideband SQUID electronics with 16-MHz flux modulation were developed using a resonant superconducting thin-film transformer [64] or a non-resonant terminated transmission-line transformer [65]. A closed loop bandwidth exceeding 2.5 MHz and a slew rate greater than 1 $\Phi_0/\mu s$ at frequencies up to 1 MHz were reported in [64], which are roughly consistent with the dead time $t_d \approx$ 100 ns deduced from the measured phase response. An even higher modulation frequency of 33 MHz was reported for a high-T_c system involving two transformers and 56 cm long 50 Ω cables between 77 K and 300 K [66]. This high modulation frequency enabled an FLL bandwidth of 10 MHz and slew rates of up to about 10 $\Phi_0/\mu s$ which are record values for flux modulated systems. However, modulation frequencies substantially above 1 MHz are inconvenient in practice due to increased complexity and high demands on the wiring between the cryogenic part and the room temperature electronics. Therefore, flux-modulated SQUIDs are commonly operated at modulation frequencies well below 1 MHz.

C.   Direct Readout

In the early 1990s, direct readout schemes without flux modulation were developed, stimulated by the need to simplify the electronics of biomagnetic multichannel systems [51,53,67,68]. Nowadays, direct readout is widely used, in particular when applying SQUIDs as preamplifiers for superconducting detectors. Over the past decades, various concepts for amplifier noise reduction were introduced by different research groups. This has lead to a quite confusing diversity of acronyms and notations. Recently, a general approach for understanding and analyzing direct readout schemes for SQUIDs was published [69]. It was pointed out that all existing methods for suppression of room temperature amplifier noise are based on feeding the SQUID voltage and/or current back into the SQUID loop. Voltage and current feedback were introduced in the early 1990s under the names *additional positive feedback* (APF) [53] and *bias current feedback* (BCF) [51], respectively. It was further shown in [69] that direct SQUID readout schemes can be conveniently analyzed by considering the SQUID and the amplifier separately. This approach allows an intuitive understanding of the various readout concepts reported in literature, and leads to simple mathematical expressions for the expected overall behavior.

It was stressed in [69] that the noise suppression does not depend on the way the SQUID is biased (constant current or voltage). The bias mode can be selected independently from the noise optimization according to the requirements in dynamic range and linearity. Current bias is more straightforward, but voltage bias yields a better intrinsic linearity of the SQUID and thus a better slew rate at given bandwidth. For wideband systems, the cable between the SQUID and the amplifier should be terminated (or at least be resistively shunted). This means that wideband system commonly apply neither ideal current bias nor ideal voltage bias, but rather a mixture of both.

Preamplifier voltage noise commonly makes direct readout of single SQUIDs impossible. To circumvent this problem, voltage feedback was introduced in 1990 under the name APF and applied to a current-biased SQUID magnetometer [53]. Subsequently, it was utilized for a voltage-biased SQUID [67] and later named *noise cancellation* (NC) scheme [68]. The basic voltage feedback circuit is depicted in Fig. 16(a). It consists of a resistor R_A and a coil L_A in series, both connected in parallel to the SQUID. The coil L_A is magnetically coupled to the SQUID via a mutual inductance M_A. Assuming that the SQUID is biased at a working point W at the positive slope of the V-Φ characteristic, a positive change in flux $\delta\Phi$ will cause a positive voltage change δV. The resulting increase of the current in the coil L_A induces an additional, positive flux in the SQUID via M_A which increases the SQUID voltage further and leads to an enhanced transfer coefficient V_Φ. Similarly, the transfer coefficient is lowered when W is located at the negative slope of the V-Φ characteristic. Therefore, the V-Φ characteristic becomes strongly asymmetric as schematically shown in Fig. 16(a). The I-Φ characteristic, however, is not affected by voltage feedback since it is measured at constant SQUID voltage and thus at constant current through the feedback coil L_A.

With voltage feedback, the transfer coefficient V_Φ can be sufficiently boosted to make the amplifier voltage noise contribution smaller than the intrinsic SQUID noise. The peak-peak voltage swing V_{pp} is somewhat reduced because R_A resistively loads the SQUID. Thermal noise in R_A causes some extra flux noise in the SQUID which is acceptable if R_A has the same operation temperature as the SQUID (typically R_A is integrated on the SQUID chip). It was shown that for adequate dimensioning ($R_A \approx 2.5R$) the increase in the noise energy ε due to

voltage feedback is about half the theoretical value according to Eq. (5) [3].

As generally the case, positive feedback leads to a bandwidth reduction. This is not a severe limitation in practice since the feedback circuit is commonly integrated on the sensor chip and has a sufficiently high bandwidth. For a current-biased SQUID, the reduction in the intrinsic linearity Φ_{pp} leads to a degradation in slew rate. However, this is often acceptable because the bandwidth with direct readout is rather high. With voltage bias the slew rate is not degraded because the I-Φ characteristic is not affected. If the voltage feedback is made too strong, hysteresis occurs in the V-Φ characteristic. Due to wideband noise "smearing" out the hysteresis, the onset of hysteresis might not be recognized in the experimental setup and a too high feedback gain might be chosen. This can result in excess noise from random switching, although the measured V-Φ characteristic may look smooth and non-hysteretic.
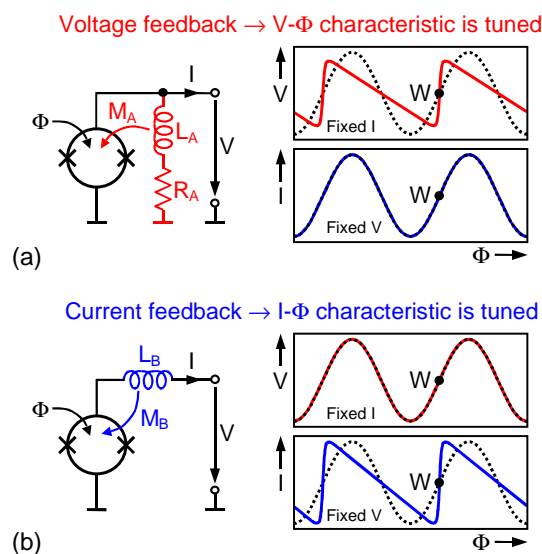
Fig. 16. Basic circuits for (a) voltage feedback and (b) current feedback. The SQUID characteristics without feedback (dotted lines) and with feedback (solid lines) are schematically depicted on the right side. With voltage feedback the swing in the V-Φ characteristic is reduced because R_A resistively loads the SQUID, whereas with current feedback the full swing is preserved. The working points W yield positive feedback in both cases (a) and (b). The flux offsets are chosen such that the working points without and with feedback coincide.

There are other methods to obtain a large voltage transfer coefficient, for example using SQUIDs with weakly shunted Josephson junctions operated near the hysteresis limit [59,70] or SQUIDs with unshunted junctions based on relaxation oscillations [71]. Although the V-Φ characteristics remain symmetric in these cases, the intrinsic linearity Φ_{pp} is reduced compared to a standard SQUID. Only SSAs offer large transfer coefficients combined with highest possible linearity. If it is unavoidable to increase the transfer coefficient at the detriment of linearity, the feedback gain should not be chosen unnecessarily high but just high enough to obtain an acceptable amplifier noise contribution.

For direct readout of single SQUIDs, preamplifier current noise is generally not critical except in the low-frequency regime or at very high frequencies where the current noise of semiconductor amplifiers typically increases. Current noise was completely disregarded in the early phase of direct SQUID readout [53,67]. However, a few years later it became an issue at PTB due to relatively high-ohmic SQUID magnetometers and a high $1/f$ noise level of the amplifiers used at this time (Linear Technology LT1028). As a countermeasure, current

feedback was introduced under the name BCF [51]. The corresponding circuit is depicted in Fig. 16(b). A coil L_B (which is connected in series to the SQUID) is magnetically coupled to the SQUID loop via a mutual inductance M_B. For the analysis we assume positive feedback at the chosen working point W. If the current changes by a small amount δI, the resulting voltage change via the magnetic coupling $V_\Phi M_B \delta I$ will be added to the voltage change $-R_{dyn}\delta I$ resulting from the SQUID's dynamic resistance. Converting the total voltage change into flux one obtains $\delta\Phi = (M_B - M_{dyn})\delta I$. The total flux change becomes zero for $M_B = M_{dyn}$ which means zero dynamic resistance of the SQUID with current feedback and complete suppression of amplifier current noise. In other words, the transfer coefficient of the I-Φ characteristic $I_\Phi = \partial I/\partial\Phi$ becomes infinite.

We conclude that both voltage and current feedback lead to strongly asymmetric characteristics with substantially boosted transfer coefficient V_Φ or I_Φ at the slope with positive feedback. Note that in Fig. 16 the direction of the current I is reversed as in [69] contrary to the normal convention. With reversed current direction optimum amplifier noise suppression always occurs for positive feedback so that the similarity of voltage and current feedback can be demonstrated more clearly.

Complementary to voltage feedback, current feedback modifies the I-Φ characteristic but does not affect the V-Φ characteristic. In contrast to voltage feedback, there is no reduction in the current swing and no excess flux noise. However, wideband noise may distort the SQUID characteristic similar to the case with voltage feedback (in particular for SQUIDs with high inductance). It is advisable to connect a resistor R_B in parallel to the feedback coil L_B in order to limit the feedback bandwidth [51]. The extra flux noise due to thermal noise in R_B is typically insignificant. Feeding the bias current asymmetrically into the SQUID has a similar effect as current feedback. In this case, half of the SQUID inductance L acts as an "intrinsic" feedback coil with an effective mutual inductance $M_B = \pm L/2$ [72]. Most SQUID sensors developed at PTB are equipped with this technique to reduce the dynamic resistance at "no expense."

Current feedback is also well suited for a two-stage SQUID to increase the flux gain between the first and the second stage. This was first demonstrated in [38] under the somewhat misleading acronym APF (which was at this time not considered as a synonym for voltage feedback but rather used to indicate that the additional feedback was positive). PTB's two-stage sensor are normally equipped with current feedback (see Fig. 10). Using negative instead of positive current feedback, the linearity of a SQUID or SSA can be increased to enable operation without room temperature FLL. This technique was introduced independently by two research groups under the names *output current feedback* (OCF) [60] and *current-sampling feedback* [73].

Voltage and current feedback can be combined for maximum suppression of amplifier noise. This was first demonstrated in 1993 for an integrated multiloop magnetometer with current bias [51]. This particular device involved a special design where the feedback resistor R_A is merged into the junction shunt resistors and only one feedback coil is used to realize the functions of L_A and L_B. A combination of voltage and current feedback was recently applied to a voltage biased SQUID and published under the name *SQUID bootstrap circuit* (SBC) [74]. A description of the different implementations is given in [69].

With direct readout a high bandwidth can easily be obtained because there is no limiting modulation frequency and the loop delay can be made very small. The first system with voltage feedback, published in 1990 [53], achieved a bandwidth of 0.5 MHz. Five years later, the bandwidth was increased to 5 MHz [75], comparable to the fastest systems with flux

modulation at this time. Another factor of 3 improvement to 15 MHz was achieved in the following two years [76]. Since then, there was only slight improvement to 20 MHz bandwidth [59] because the overall FLL performance is limited by the loop delay in the wiring between the cryogenic part and the room temperature electronics. Several 100 MHz bandwidth were demonstrated with "cold" FLL electronics [38] or on-chip feedback by large SQUID arrays [60], but these techniques have not become established. In contrast, direct readout electronics with a bandwidth $\gtrsim 5$ MHz are nowadays commercially available and widely used. The noise spectra shown as examples in this chapter were measured with the commercial variant of the electronics in [59] (XXF-1 from Magnicon GmbH, Hamburg) and include the noise contribution from the preamplifier.

IV.   CONCLUSIONS

We are looking back to half a century of SQUID history. The initial devices were made from machined bulk Nb with point contact junctions realized by screws. A big step forward was the advent of reliable thin-film tunnel junction processes in the 1980s, predominantly the Nb-AlOx-Nb trilayer technology. In the beginning, the development of SQUIDs was mainly driven by biomagnetism. The need for large biomagnetic multichannel systems initiated a rapid development of SQUID concepts and readout schemes, in particular in the 1990s. At the same period another important field emerged, the use of SQUIDs as preamplifiers for superconducting detectors.

Today, SQUID technology has become mature. Modern Nb-based devices are extremely sensitive, versatile and robust, but their main restriction is the need for cryogenic temperatures. Nevertheless, SQUIDs are widely used in biomagnetism, astronomy, geomagnetism, material sciences, and metrology. Many interesting experiments in fundamental research became possible thanks to the SQUID's ultimate sensitivity. SQUID current sensors are used as preamplifiers for large detector arrays, for example SCUBA-2 with more than ten thousand TES bolometer pixels. Numerous large biomagnetic multichannel systems with sophisticated noise cancellation techniques are operated worldwide, partially in clinical environment. These systems are commercially available as well as small-scale laboratory SQUIDs, where the user can individually design the pickup circuit for his specific application. Although being a small component in the whole system, the SQUID decisively determines the overall system performance. An example is the magnetic property measurement system, probably the best-seller in SQUID-based instruments. Being equipped with a cryocooler, the user has not to care about cryogenic cooling. The user-friendliness of SQUID-based instruments has also been greatly improved in the past decades. Nowadays, systems are inevitably fully computer controlled and operable even for non-scientists.

ACKNOWLEDGEMENTS

REFERENCES

[1] Ryhänen, T., Seppä, H., Ilmoniemi, R. and Knuutila, K. (1989). SQUID magnetometers for low-frequency applications, *J. Low Temp. Phys.* **76**, pp. 287-386.

[2] Barone, A., ed. (1992) *Principles and Applications of Superconducting Quantum Interference Devices* (World Scientific Publishing, Singapore).

[3] Weinstock, H., ed. (1996) *SQUID Sensors: Fundamentals, Fabrication and Applications*, NATO ASI series E: Applied Sciences, Vol. 329 (Kluwer Academic Publishers, Dordrecht).

[4] Clarke, J. and Braginski, A. I., eds. (2004) *The SQUID Handbook* Vol. I: Fundamentals and Technology of SQUIDs and SQUID Systems (Wiley-VCH, Weinheim).

[5] Clarke, J. and Braginski, A. I., eds. (2006) *The SQUID Handbook* Vol. II: Applications of SQUIDs and SQUID Systems (Wiley-VCH, Weinheim).

[6] Seidel, P., ed. (2015) *Applied Superconductivity* Vol. 2, Chapter 9 "Superconducting Quantum Interference (SQUIDs)" (Wiley-VCH, Weinheim) pp. 949-1110.

[7] Jaklevic, R. C., Lambe, J., Silver, A. H. and Mercereau, J. E. (1964). Quantum interference effects in Josephson tunneling, *Phys. Rev. Lett.* **12**, pp. 159-160.

[8] Zimmerman, J. E. and Silver, A. H. (1966). Macroscopic quantum interference effects through superconducting point contacts, *Phys. Rev.* **141**, pp. 367-375.

[9] Stewart, W. C. (1968). Current-voltage characteristics of Josephson junctions, *Appl. Phys. Lett.* **12**, pp. 277-280.

[10] McCumber, D. E. (1968). Effect of ac impedance on dc voltage-current characteristics of superconductor weak-link junctions, *J. Appl. Phys.* **39**, pp. 3113-3118.

[11] Anders, S., Schmelz, M., Fritzsch, L., Stolz, R., Zakosarenko, V., Schönau, T. and Meyer, H.-G. (2009). Sub-micrometer-sized, cross-type Nb-AlOx-Nb tunnel junctions with low parasitic capacitance, *Supercond. Sci. Technol.* **22**, 064012 (4 pp).

[12] Granata, C and Vettoliere, A. (2016). Nano superconducting quantum interference device: A powerful tool for nanoscale investigations, *Physics Reports* **614**, pp. 1-69.

[13] Tesche, C. D. and Clarke, J. (1977). dc SQUID: Noise and optimization, *J. Low Temp. Phys.* **29**, pp. 301-331.

[14] Bruines, J. J. P., de Waal, V. J. and Mooij, J. E. (1982). Comment on: "dc SQUID: Noise and optimization" by Tesche and Clarke, *J. Low Temp. Phys.* **46**, pp. 383-386.

[15] de Waal, V. J., Schrijner, P. and Llurba R. (1982). Simulation and optimization of a dc SQUID with finite capacitance, *J. Low Temp. Phys.* **54**, pp. 215-232.

[16] Ryhänen, T., Seppä, H. and Cantor., R. (1992). Effect of parasitic capacitance and inductance on the dynamics and noise of dc superconducting quantum interference devices, *J. Appl. Phys.* **71**, pp. 6150-6166.

[17] Voss, R. F. (1981). Noise characteristics of an ideal shunted Josephson junction, *J. Low Temp. Phys.* **42**, pp. 151-163.

[18] Tesche, C. D. and Clarke, J. (1979). dc SQUID: Current noise, *J. Low Temp. Phys.* **37**, pp. 397-403.

[19] Martinis, J. M. and Clarke, J. (1986). Current noise measured in the dc SQUID, *J. Low Temp. Phys.* **65**, pp. 459-468.

[20] Drung, D. (1995). Theory for the multiloop dc superconducting quantum interference device magnetometer and experimental verification, *J. Appl. Phys.* **77**, pp. 4088-4098.

[21] Enpuku, K., Yoshida, K. and Kohjiro, S. (1986). Noise characteristics of a dc SQUID with a resistively shunted inductance. II. Optimum damping, *J. Appl. Phys.* **60**, pp. 4218-4223.

[22] Knuutila, J., Ahonen, A. and Tesche, C. (1987). Effects on dc SQUID characteristics of damping of input coil resonances, *J. Low Temp. Phys.* **68**, pp 269-284.

[23] Knuutila J., Kajola, M., Seppä, H., Mutikainen, R. and Salmi, J. (1988) Design, optimization, and construction of a dc SQUID with complete flux transformer circuits, *J. Low Temp. Phys.* **71**, pp. 369-392.

[24] Drung, D., Beyer, J., Storm, J.-H., Peters, M. and Schurig, T. (2011). Investigation of low-frequency excess flux noise in dc SQUIDs at mK temperatures, *IEEE Trans. Appl. Supercond.* **21**, pp. 340-344.

[25] Wellstood, F. C., Urbina, C. and Clarke, J. (1994). Hot-electron effect in metals, *Phys. Rev. B* **49**, pp. 5942-5955.

[26] Wellstood, F. C., Urbina, C. and Clarke, J. (1987). Low-frequency noise in dc superconducting quantum interference devices below 1 K, *Appl. Phys. Lett.* **50**, pp. 772-774.

[27] Kempf, S., Ferring, A., Fleischmann A. and Enss C. (2015). Direct-current superconducting quantum

interference devices for the readout of metallic magnetic calorimeters, *Supercond. Sci. Technol.* **28**, 045008 (12 pp).

[28] Ketchen, M. B., Stawiasz, K. G., Pearson, D. J., Brunner, T. A., Hu, C.-K., Jaso, M. A., Manny, M. P., Parsons A. A. and Stein K. J. (1992). Sub-μm linewidth input coils for low T_c integrated thin-film dc superconducting quantum interference devices, *Appl. Phys. Lett.* **61**, pp. 336-338.

[29] Jaycox, J. M. and Ketchen, M. B. (1981). planar coupling scheme for ultra low noise dc SQUIDs, *IEEE Trans. Magn.* **17**, pp. 400-403.

[30] Ketchen, M. B. (1987). Integrated thin-film dc SQUID sensors, *IEEE Trans. Magn.* **23**, pp. 1650-1657.

[31] Ketchen, M. B., Gallagher, W. J., Kleinsasser, A. W. and Murphy, S. (1985). dc SQUID flux focuser, *SQUID '85, Superconducting Quantum Interference Devices and their Applications*, eds. Hahlbohm, H. D. and Lübbig, H. (Walter de Gruyter, Berlin) pp. 865-871.

[32] Drung, D., Beyer, J., Matz, H., Lindström, M., Ludwig, F. and Schurig, T. (1998). Magnetic coupling, effective area, and inductance of SQUID sensors: New theoretical description and comparison with experiment, presented at *Applied Superconductivity Conference ASC1998*, Palm Desert, CA, USA (unpublished).

[33] Drung, D. and Koch, H. (1994).An integrated dc SQUID magnetometer with variable additional positive feedback, *Supercond. Sci. Technol.* **7**, pp. 242-245.

[34] Jansman, A. B. M. (1999). High-T_c dc SQUIDs for use in a background field, *Dissertation* (University of Twente, Low Temperature Division, The Netherlands).

[35] Yoshida, K., Hossain, M. S., Kisu, T., Enpuku, K. and Yamafuji, K. (1992). Modeling of kinetic-inductance coplanar stripline with NbN thin films, *Jpn. J. Appl. Phys.* **31**, pp. 3844-3850.

[36] Grover, F. W. (1962) *Inductance Calculations: Working Formulas and Tables* (Dover, New York).

[37] Welty, R. P. and Martinis, J. M. (1991). A series array of dc SQUIDs, *IEEE Trans. Magn.* **27**, pp. 2924-2926.

[38] Drung, D., Assmann, C., Beyer, J., Kirste, A., Peters, M., Ruede, F. and Schurig, T. (2007). Highly sensitive and easy-to-use SQUID sensors, *IEEE Trans. Appl. Supercond.* **17**, pp. 699-704.

[39] Stawiasz, K. G. and Ketchen, M. B. (1993). Noise measurements of series SQUID arrays, *IEEE Trans. Appl. Supercond.* **3**, pp. 1808-1811.

[40] Stan, G., Field, S. B. and Martinis, J. M. (2004). Critical field for complete vortex expulsion from narrow superconducting strips, *Phys. Rev. Lett.* **92**, 097003 (4 pp).

[41] Carelli, P., Castellano, M. G., Flacco, K., Leoni, R. and Torrioli, G. (1997). An absolute magnetometer based on dc superconducting quantum interference devices, *Europhys. Lett.* **39**, pp. 569-574.

[42] Häussler, Ch., Oppenländer, J. and Schopohl, N. (2001). Nonperiodic flux to voltage conversion of series arrays of dc superconducting quantum interference devices, *J. Appl. Phys.* **89**, pp. 1875-1879.

[43] Beyer, J. and Drung, D. (2008). A SQUID series array dc current sensor, *Supercond. Sci. Technol.* **21**, 095012 (6 pp).

[44] Dettmann, F., Richter, W., Albrecht, G. and Zahn, W. (1979). A monolithic thin film dc-SQUID, *Phys. Stat. Sol. (a)* **51**, pp. K185-K188.

[45] Cromar, M. W. and P. Carelli, P. (1981) Low-noise tunnel junction dc SQUIDs, *Appl. Phys. Lett.* 38, pp. 723-725.

[46] Ketchen, M. B. and Jaycox, J. M. (1982). Ultra-low-noise tunnel junction dc SQUID with a tightly coupled planar input coil, *Appl. Phys. Lett.* **40**, 736-738.

[47] Carelli, P., Castellano, M. G., Torrioli, G. and Leoni, R. (1998). Low noise multiwasher superconducting interferometer, *Appl. Phys. Lett.* **72**, 115-117.

[48] Muhlfelder, B., Johnson, W. and Cromar, M. W. (1983). Double transformer coupling to a very low noise SQUID, *IEEE Trans. Magn.* **19**, pp. 303-307.

[49] ter Brake, H. J. M., Fleuren, F. H., Ulfman, J. A. and Flokstra J. (1986). Elimination of flux-transformer crosstalk in multichannel SQUID magnetometers, *Cryogenics* **26**, pp. 667-670.

[50] Hilbert, C., Clarke, J., Sleator, T. and Hahn, E. L. (1985). Nuclear quadrupole resonance detected at 30 MHz with a dc superconducting quantum interference device, *Appl. Phys. Lett.* 47, pp. 637-639.

[51] Drung, D. and Koch, H. (1993). An electronic second-order gradiometer for biomagnetic applications in clinical shielded rooms, *IEEE Trans. Appl. Supercond.* **3**, pp. 2594-2597.

[52] Zimmerman, J.E. (1971). Sensitivity enhancement of superconducting quantum interference devices through the use of fractional-turn loops, *J. Appl. Phys.* **42**, pp. 4483-4487.

[53] Drung, D., Cantor, R., Peters, M., Scheer, H. J. and Koch, H. (1990). Low-noise high-speed dc superconducting quantum interference device magnetometer with simplified feedback electronics, *Appl. Phys. Lett.* **57**, 406-408.

[54] Schmelz, M., Stolz, R., Zakosarenko, V., Schönau, T., Anders, S., Fritzsch, L., Mück, M. and Meyer, H.-G. (2011). Field-stable SQUID magnetometer with sub-fT Hz$^{-1/2}$ resolution based on sub-micrometer cross-type Josephson tunnel junctions, *Supercond. Sci. Technol.* **24**, 065009 (5 pp).

[55] Dössel, O., David, B., Fuchs, M., Kullmann, W. H. and Lüdeke, K. M. (1991). A modular low noise 7-channel SQUID-magnetometer, *IEEE Trans. Magn.* **27**, pp. 2797-2800.

[56] Daalmans, G. M., Bär, L., Bömmel, F. R., Kress, R. and Uhl, D. (1991). Ultra low noise all niobium dc-SQUIDs, *IEEE Trans. Magn.* **27**, pp. 2997-3000.

[57] Bechstein, S., Ruede, F., Drung, D., Storm, J.-H., Kieler, O. F., Kohlmann, J., Weimann, T. and Schurig, T. (2015). HfTi-nanoSQUID gradiometers with high linearity, *Appl. Phys. Lett.* **106**, 072601 (4 pp).

[58] Drung, D. (2003). High-T_c and low-T_c dc SQUID electronics, *Supercond. Sci. Technol.* **16**, pp. 1320-1336.

[59] Drung, D., Hinnrichs, C. and Barthelmess, H.-J. (2006). Low-noise ultra-high-speed dc SQUID readout electronics, *Supercond. Sci. Technol.* **19**, S235-S241.

[60] Drung, D., Beyer, J., Peters, M., Storm, J.-H. and Schurig, T. (2009). Novel SQUID current sensors with high linearity at high frequencies, *IEEE Trans. Appl. Supercond.* **19**, pp. 772-777.

[61] Forgacs, R. L. and Warnick, A. (1967). Digital-analog magnetometer utilizing superconducting sensor, *Rev. Sci. Instrum.* **38**, pp. 214-220.

[62] Clarke, J., Goubau, W. M. and Ketchen, M. B. (1976). Tunnel junction dc SQUID: Fabrication, operation, and performance, *J. Low Temp. Phys.* **25**, pp. 99-144.

[63] Wellstood, F., Heiden, C. and Clarke, J. (1984). Integrated dc SQUID magnetometer with a high slew rate, *Rev. Sci. Instrum.* **55**, 952-957.

[64] Koch, R. H., Rozen, J. R., Wöltgens, P., Picunko, T., Goss, W. J., Gambrel, D., Lathrop, D., Wiegert, R. and Overway, D. (1996). High performance superconducting quantum interference device feedback electronics, *Rev. Sci. Instrum.* **67**, pp. 2968-2976.

[65] Penny, R. D., Lathrop, D. K., Thorson, B. D., Whitecotton, B. R., Koch, R. H. and Rosen, J. R. (1997). Wideband front end for high-frequency SQUID electronics, *IEEE Trans. Appl. Supercond.* **7**, pp. 2323-2326.

[66] Matlashov, A., Espy, M., Kraus, Jr., R. H., Ganther, Jr., K. R. and Snapp, L. D. (2001). Electronic gradiometer using HTc SQUIDs with fast feedback electronics, 876-879.

[67] Seppä, H., Ahonen, A., Knuutila, J., Simola, J. and Vilkman, V. (1991). dc-SQUID electronics based on adaptive positive feedback: experiments, *IEEE Trans. Magn.* **27**, pp. 2488-2490.

[68] Kiviranta, M. and Seppä, H. (1995) dc SQUID electronics based on the noise cancellation scheme, *IEEE Trans. Appl. Supercond.* **5**, pp. 2146-2148.

[69] Drung, D. (2010). Simplified analysis of direct SQUID readout schemes, *Supercond. Sci. Technol.* **23**, 065006 (7 pp)

[70] Polushkin, V., Glowacka, D., Hart, R. and Lumley, J. (1999). Effect of an input coil microwave resonance on dynamics and noise properties of a dc superconducting quantum interference device operating close to the hysteretic mode, *Rev. Sci. Instrum.* **70**, 1713-1718.

[71] Adelerhof, D. J., Nijstad, H., Flokstra, J. and Rogalla, H. (1994). (Double) relaxation oscillation SQUIDs with high flux-to-voltage transfer: simulations and experiments, *J. Appl. Phys.* **76**, pp. 3875-3886.

[72] Uehara, G., Matsuda, N., Kazami, K., Takada, Y. and Kado, H. (1993). Asymmetric bias injection technique for Drung-type superconducting quantum interference devices, *Japan. J. Appl. Phys.* **32**, L1735-L1738.

[73] Kiviranta, M. (2008) SQUID linearization by current-sampling feedback, *Supercond. Sci. Technol.* **21** 045009 (6 pp).

[74] Xie, X., Zhang, Y., Wang, H., Wang, Y., Mück, M., Dong, H., Krause, H.-J., Braginski, A. I., Offenhäusser, A. and Jiang, M. (2010). Voltage biased superconducting quantum interference device bootstrap circuit *Supercond. Sci. Technol.* **23**, 065016 (4 pp).

[75] Drung, D., Matz, H. and Koch, H. (1995). A 5-MHz bandwidth SQUID magnetometer with additional positive feedback, *Rev. Sci. Instrum.* **66**, pp. 3008-3015.

[76] Drung, D. (1997). Improved dc SQUID read-out electronics with low 1/*f* noise preamplifier, *Rev. Sci. Instrum.* **68**, pp. 4066-4074.